A statistical state dynamics-based study of the structure and mechanism of large-scale motions in plane Poiseuille flow

Brian F. Farrell[1], Petros J. Ioannou[2,†], Javier Jiménez[3],
Navid C. Constantinou[4], Adrián Lozano-Durán[3,‡] and
Marios-Andreas Nikolaidis[2]

[1]Department of Earth and Planetary Sciences, Harvard University, Cambridge, MA 02138, USA

[2]Department of Physics, National and Kapodistrian University of Athens, Panepistimiopolis, Zografos, Athens, 157 84, Greece

[3]School of Aeronautics, Universidad Politécnica de Madrid, 28040, Madrid, Spain

[4]Scripps Institution of Oceanography, University of California San Diego, La Jolla, CA 90293-0213, USA

The perspective of statistical state dynamics (SSD) has recently been applied to the study of mechanisms underlying turbulence in a variety of physical systems. An SSD is a dynamical system that evolves a representation of the statistical state of the system. An example of an SSD is the second-order cumulant closure referred to as stochastic structural stability theory (S3T), which has provided insight into the dynamics of wall turbulence, and specifically the emergence and maintenance of the roll/streak structure. S3T comprises a coupled set of equations for the streamwise mean and perturbation covariance, in which nonlinear interactions among the perturbations has been removed, restricting nonlinearity in the dynamics to that of the mean equation and the interaction between the mean and perturbation covariance. In this work, this quasi-linear restriction of the dynamics is used to study the structure and dynamics of turbulence in plane Poiseuille flow at moderately high Reynolds numbers in a closely related dynamical system, referred to as the restricted nonlinear (RNL) system. Simulations using this RNL system reveal that the essential features of wall-turbulence dynamics are retained. Consistent with previous analyses based on the S3T version of SSD, the RNL system spontaneously limits the support of its turbulence to a small set of streamwise Fourier components, giving rise to a naturally minimal representation of its turbulence dynamics. Although greatly simplified, this RNL turbulence exhibits natural-looking structures and statistics, albeit with quantitative differences from those in direct numerical simulations (DNS) of the full equations. Surprisingly, even when further truncation of the perturbation support to a single streamwise component is imposed, the RNL system continues to self-sustain turbulence with qualitatively realistic structure and dynamic properties. RNL turbulence at the Reynolds numbers studied is dominated by the roll/streak structure in the buffer layer and similar very large-scale structure (VLSM) in the

† Email address for correspondence: pjioannou@phys.uoa.gr
‡ Present address: Center for Turbulence Research, Stanford University, Stanford, CA 94305, USA.

outer layer. In this work, diagnostics of the structure, spectrum and energetics of RNL and DNS turbulence are used to demonstrate that the roll/streak dynamics supporting the turbulence in the buffer and logarithmic layer is essentially similar in RNL and DNS.

Key words: boundary layer structure, parametric instability, turbulence theory

---

1. Introduction

The fundamental importance of the roll/streak structure in the dynamics of wall turbulence was recognized soon after it was observed in the near-wall region in boundary layer flows (Hama, Long & Hegarty 1957; Kline *et al.* 1967) and seen in early direct numerical simulations (DNS) of channel flows (cf. Kim, Moin & Moser 1987). Recently, in both experiments and numerical simulations of turbulent flows at high Reynolds numbers, roll/streak structures have been identified in the logarithmic layer with self-similar scale increasing with the distance from the wall (del Álamo *et al.* 2006; Hellström, Sinha & Smits 2011; Lozano-Durán, Flores & Jiménez 2012; Lozano-Durán & Jiménez 2014*b*; Hellström, Marusic & Smits 2016). Further from the wall, similar very large streak structures are seen that scale with the channel half-height or pipe radius, h, or with the boundary layer thickness, δ (Bullock, Cooper & Abernathy 1978; Jiménez 1998; Kim & Adrian 1999). These coherent motions are variously referred to as superstructures or very large-scale motions (VLSM) (del Álamo *et al.* 2004; Toh & Itano 2005; Hutchins & Marusic 2007; Marusic *et al.* 2010).

In this paper the mechanism maintaining these large and very large-scale structures in the upper layers of turbulent plane Poiseuille flow is studied by making use of the methods of statistical state dynamics (SSD) with averaging operator the streamwise average. Conveniently, the fundamental dynamics of wall turbulence is contained in the simplest non-trivial SSD: a second-order closure of the equations governing the cumulants of the full SSD, referred to as the stochastic structural stability theory (S3T) system (Farrell & Ioannou 2003, 2012). Restriction of the dynamics to the first two cumulants involves either parameterizing the third cumulant by stochastic excitation or, as we will adopt in this work, setting it to zero. With the chosen streamwise averaging operator, the first cumulant or mean flow is the streamwise-averaged flow, i.e. the flow component with streamwise wavenumber $k_x = 0$, and the second cumulant is the covariance of the perturbations, which are defined as the deviations from the mean, i.e. the flow components with wavenumber $k_x \neq 0$. Either stochastic parameterization or setting the third cumulant to zero results in a quasi-linear dynamics in which perturbation–perturbation interactions are not explicitly calculated (cf. figure 1). We refer to this quasi-linear approximation to the Navier–Stokes equations (NS) used in S3T as the RNL (restricted nonlinear) approximation. The RNL equations are derived from the NS by making the same dynamical restriction as that of S3T. A significant consequence of the S3T and RNL restriction to the NS dynamics is the elimination of the classical perturbation–perturbation turbulent cascade.

This second-order closure has been justified by Bouchet, Nardini & Tangarife (2013) in the limit $\lambda\tau \ll 1$, where τ is the shear time scale of the large-scale flow and $1/\lambda$ the relaxation time associated with damping of the large-scale flow. However, S3T theory is predictive even when $\lambda\tau \gg 1$. For example, it predicts the bifurcation from

the statistically homogeneous to the inhomogeneous state that has been confirmed using DNS both in barotropic turbulence (Constantinou, Farrell & Ioannou 2014*a*) and three-dimensional Couette flow turbulence (Farrell, Ioannou & Nikolaidis 2016).

The S3T closure had been used to study large-scale coherent structure dynamics in planetary turbulence (Farrell & Ioannou 2003, 2007, 2008, 2009*a*,*c*; Marston, Conover & Schneider 2008; Srinivasan & Young 2012; Bakas & Ioannou 2013; Constantinou *et al.* 2014*a*; Parker & Krommes 2014; Constantinou, Farrell & Ioannou 2016) and drift-wave turbulence in plasmas (Farrell & Ioannou 2009*b*; Parker & Krommes 2013). At low Reynolds numbers the S3T closure of wall-bounded turbulence has been shown to provide a theoretical framework predicting the emergence and maintenance of the roll/streak structure in transitional flows as well as the mechanism sustaining the turbulent flow subsequent to transition. In particular, S3T predicts a new mechanism for the emergence of the roll/streak structure in pre-transitional flow through a free-stream-turbulence-induced modal instability and its equilibration at finite amplitude. In addition, S3T provides a theory for maintenance of turbulence through a time-dependent parametric instability process after transition (Farrell & Ioannou 2012). (Parametric instability traditionally refers to the instability of a linear non-autonomous system, a parameter of which varies periodically in time (cf. Drazin & Reid 1981, § 48). We generalize the concept of parametric instability to include any linear instability that is inherently caused by the time dependence of the system. The reason we have adopted the same term to refer to the instability induced by time dependence in both periodic and non-periodic systems is that the same mechanism underlies the instability in these systems, which is the inherent non-normality of non-commuting time-dependent systems coupled with the convexity of the exponential function (cf. Farrell & Ioannou 1996*b*, 1999).)

In S3T the perturbation covariance is obtained directly from a Lyapunov equation which is equivalent to obtaining the covariance as an ensemble mean of the perturbation covariances obtained from an infinite ensemble of RNL perturbation equations sharing the same mean flow. In the RNL system used in this work, the Reynolds stresses are obtained from the covariance formed using a single member perturbation ensemble. Using a single member of the perturbation ensemble to directly calculate the Reynolds stresses bypasses explicit formation of the perturbation covariance and, in this way, it has the advantage over S3T that it can be easily implemented at high resolution in a DNS (cf. Constantinou *et al.* 2014*b*; Thomas *et al.* 2014).

S3T has allowed formulation of new theoretical constructs for understanding the dynamics of turbulence, but is restricted in application to moderate Reynolds numbers by the necessity to solve explicitly for the perturbation covariance. RNL, by inheriting the structure of S3T, allows extension of S3T methods of analysis to much higher Reynolds numbers. While the perturbation variables that appear in the RNL equations are the velocities, for the purposes of making contact with the theoretical results of S3T analysis it is important to take the additional conceptual step of regarding the perturbation variable of RNL to be the covariance associated with these perturbation variables which is an approximation to the exact perturbation covariance of S3T. Taking this perspective underscores and makes explicit the parallelism between the S3T exact statistical state dynamics and the RNL approximation to it.

In order to maintain turbulence in wall-bounded shear flow, a mechanism is required to transfer kinetic energy from the external forcing to the perturbations. Obtaining understanding of this mechanism is a fundamental challenge in developing a comprehensive theory of turbulence in these flows. If the mean flow were stationary

and inflectional then fast hydrodynamic linear instabilities might plausibly be invoked as responsible for producing this transfer. However, most wall-bounded shear flows are both rapidly varying and not inflectional, and the mechanism of energy transfer to the perturbations involves nonlinear processes that exploit linear transient growth arising from the non-normality of the flow dynamics. The problem with sustaining turbulence using transiently growing perturbations is that these perturbations ultimately decay and must be renewed or else the turbulence is not sustained, as is familiar from the study of rapid distortion theory (Kim & Lim 2000). A mechanism that exploits nonlinearity to maintain the transiently growing perturbations we refer to as a self-sustaining process (SSP) (Hamilton, Kim & Waleffe 1995; Jiménez & Pinelli 1999; Jiménez 2013). The various SSP mechanisms that have been proposed have in common this sustaining of transient growth associated with the non-normality of the mean flow by exploiting nonlinearity to renew the transiently growing set of perturbations. Consistent with the roll/streak structure being the structure of optimal linear growth, proposed SSP mechanisms may be regarded as alternative nonlinear processes for renewing this structure (Hamilton *et al.* 1995; Hall & Sherwin 2010; Jiménez 2013). In the case of the S3T, and also in the dynamically similar RNL studied in this work, the mechanism effecting this transfer is known: it is systematic correlation by the streak of perturbation Reynolds stresses that force the roll, which in turn maintains the streak through the lift-up process. These Reynolds stresses are produced by the Lyapunov vectors arising from parametric instability of the time-dependent streak. This mechanism, which has analytical expression in S3T and in the noise-free RNL, comprises a cooperative interaction between the coherent streamwise mean flow and the incoherent turbulent perturbations. It was analysed first using S3T, and implications of this analysis, including the predicted parametric streak instability and its associated Lyapunov spectrum of modes, have been studied in subsequent work (Farrell & Ioannou 2012; Constantinou *et al.* 2014*b*; Thomas *et al.* 2014, 2015; Farrell & Ioannou 2016; Nikolaidis *et al.* 2016). This analysis of the SSP using S3T, including the parametric instability of the streak and the structure of the perturbation field arising as the leading Lyapunov vector of this parametric growth, will be frequently invoked in this work. Detailed explanation of these concepts can be found in the above references.

In this paper, we compare DNS and RNL simulations made without any explicit stochastic parameterization at relatively high Reynolds numbers in pressure-driven channel flow. Included in this comparison are flow statistics, structures, and dynamical diagnostics. This comparison allows the effects of the dynamical restriction in RNL to be studied. We find that RNL with the stochastic parameterization set to zero spontaneously limits the support of its turbulence to a small set of streamwise Fourier components, giving rise naturally to a minimal representation of its turbulence dynamics. Furthermore, the highly simplified RNL dynamics supports a self-sustaining roll/streak SSP in the buffer layer consistent with that predicted by S3T at lower Reynolds number and similar to that of DNS. Finally, we find that roll/streak structures in the log-layer are also supported by an essentially similar SSP.

2. RNL dynamics

Consider a plane Poiseuille flow in which a constant mass flux is maintained by application of a time-dependent pressure, $-G(t)x$, where x is the streamwise coordinate. The wall-normal direction is y and the spanwise direction is z. The lengths of the channel in the streamwise, wall-normal and spanwise direction are

(a) $\hat{U}(k_1 + k_2)$ (b) $\hat{U}(k_1 + k_2)$ (c) $\hat{u}'(k_1 + k_2)$ (d) $\hat{u}'(k_1 + k_2)$

$\hat{u}'(k_1)$ $\hat{u}'(k_2)$ $\hat{U}(k_1)$ $\hat{U}(k_2)$ $\hat{U}(k_1)$ $\hat{u}'(k_2)$ $\hat{u}'(k_1)$ $\hat{u}'(k_2)$
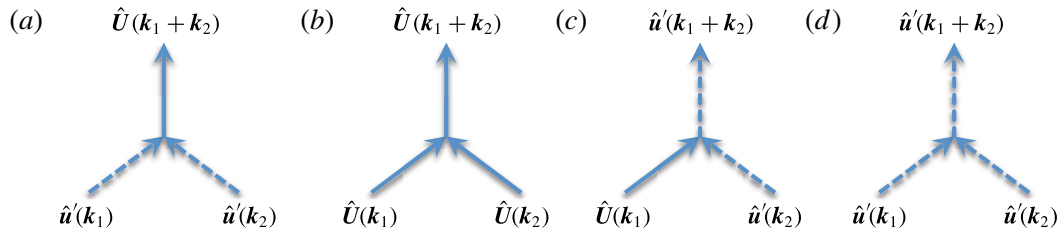
FIGURE 1. (Colour online) Nonlinear interactions that are included or excluded in the S3T and RNL approximations of the NS. Mean flow Fourier components $\hat{U}(k)$ with wavenumber $k = (0, k_y, k_z)$ are indicated with solid arrows, the perturbation Fourier components $\hat{u}'(k)$ with $k_x \neq 0$ with dashed arrows. The possible nonlinear interactions are: (a) a perturbation with streamwise wavenumber k_{x_1} interacts with another perturbation with $k_{x_2} = -k_{x_1}$ to produce a mean flow component with $k_x = 0$, (b) two mean flow components interact to make another mean flow component, (c) a mean flow component interacts with a perturbation to make a perturbation component and (d) two perturbation components with streamwise wavenumbers $k_{x_1} \neq -k_{x_2}$ interact to make another perturbation component. All interactions are included in the NS equations. Interactions (a) and (b) are included in the S3T and RNL mean equations, while in the S3T and RNL perturbation equations interactions (c) are included and interactions (d) are either neglected or stochastically parameterized.

respectively L_x, $2h$ and L_z. The channel walls are at $y/h = 0$ and 2. Averages are denoted by square brackets with a subscript denoting the variable which is averaged, e.g. spanwise averages by $[\cdot]_z = L_z^{-1} \int_0^{L_z} \cdot \, dz$, time averages by $[\cdot]_t = T^{-1} \int_0^T \cdot \, dt$, with T sufficiently long. Multiple subscripts denote an average over the subscripted variables in the order they appear, e.g. $[\cdot]_{x,y} \stackrel{def}{=} [[\cdot]_x]_y$. The velocity, u, is decomposed into its streamwise mean value, denoted by $U(y, z, t) \stackrel{def}{=} [u(x, y, z, t)]_x$, and the deviation from the mean (the perturbation), $u'(x, y, z, t)$, so that $u = U + u'$. The pressure is similarly written as $p = -G(t)x + P(y, z, t) + p'(x, y, z, t)$. The NS decomposed into an equation for the mean and an equation for the perturbation are:

$$\partial_t U + U \cdot \nabla U - G(t)\hat{x} + \nabla P - \nu \Delta U = -[u' \cdot \nabla u']_x, \qquad (2.1a)$$

$$\partial_t u' + U \cdot \nabla u' + u' \cdot \nabla U + \nabla p' - \nu \Delta u' = -(u' \cdot \nabla u' - [u' \cdot \nabla u']_x), \qquad (2.1b)$$

$$\nabla \cdot U = 0, \quad \nabla \cdot u' = 0, \qquad (2.1c,d)$$

where ν is the coefficient of kinematic viscosity. No-slip boundary conditions are applied in the wall-normal direction and periodic boundary conditions in the streamwise and spanwise directions. All nonlinear interactions among the mean flow components (flow components with streamwise wavenumber $k_x = 0$) and perturbations (flow components with streamwise wavenumber $k_x \neq 0$) in (2.1) are summarized in figure 1.

The x, y, z components of U are (U, V, W) and the corresponding components of u' are (u', v', w'). Streamwise mean perturbation Reynolds stress components are denoted as e.g. $[u'u']_x$, $[u'v']_x$. The streak component of the streamwise mean flow is denoted by U_s and defined as

$$U_s \stackrel{def}{=} U - [U]_z. \qquad (2.2)$$

The V and W are the streamwise mean velocities of the roll vortices. We also define the streak energy density, $E_s = h^{-1} \int_0^h dy (1/2)[U_s^2]_z$, and the roll energy density, $E_r = h^{-1} \int_0^h dy (1/2)[V^2 + W^2]_z$.

The RNL approximation is obtained by neglecting or parameterizing stochastically the perturbation–perturbation interaction terms in (2.1b) (cf. figure 1). In this paper we set the stochastic parameterization to zero and the RNL system becomes:

$$\partial_t \boldsymbol{U} + \boldsymbol{U} \cdot \nabla \boldsymbol{U} - G(t)\hat{\boldsymbol{x}} + \nabla P - \nu \Delta \boldsymbol{U} = -[\boldsymbol{u}' \cdot \nabla \boldsymbol{u}']_x, \tag{2.3a}$$

$$\partial_t \boldsymbol{u}' + \boldsymbol{U} \cdot \nabla \boldsymbol{u}' + \boldsymbol{u}' \cdot \nabla \boldsymbol{U} + \nabla p' - \nu \Delta \boldsymbol{u}' = 0, \tag{2.3b}$$

$$\nabla \cdot \boldsymbol{U} = 0, \quad \nabla \cdot \boldsymbol{u}' = 0. \tag{2.3c,d}$$

Equation (2.3a) describes the dynamics of the streamwise mean flow, $\boldsymbol{U}$, which is driven by the divergence of the streamwise mean perturbation Reynolds stresses. These Reynolds stresses are obtained from (2.3b), in which the streamwise-varying perturbations, $\boldsymbol{u}'$, evolve under the influence of the time-dependent streamwise mean flow $\boldsymbol{U}(y, z, t)$ with no explicitly retained interaction among these streamwise-varying perturbations (the retained interactions are shown in the diagram of figure 1). Remarkably, RNL self-sustains turbulence solely due to the perturbation Reynolds stress forcing of the streamwise mean flow (2.3a), in the absence of which a self-sustained turbulent state cannot be established (Gayme 2010; Gayme *et al.* 2010).

Because the RNL equations do not include interactions among the perturbations, and because $\boldsymbol{U}$ is streamwise constant, each component $\hat{\boldsymbol{u}}'_{k_x} e^{ik_x x}$ of perturbation velocity $\boldsymbol{u}'$ in the Fourier expansion:

$$\boldsymbol{u}'(x, y, z, t) = \sum_{k_x \in K_x} \text{Re}[\hat{\boldsymbol{u}}'_{k_x}(y, z, t)e^{ik_x x}], \tag{2.4}$$

where $K_x \stackrel{def}{=} 2\pi/L_x[1, 2, 3, \ldots, N_x/2]$ is all the positive k_x wavenumbers included in the simulation, evolves independently in (2.3b) and therefore (2.3b) can be split into independent equations for each k_x. By taking the Fourier transform of (2.3b) in x and eliminating the perturbation pressure, (2.3b) can be symbolically written as:

$$\partial_t \hat{\boldsymbol{u}}'_{k_x} = \boldsymbol{A}_{k_x}(\boldsymbol{U})\hat{\boldsymbol{u}}'_{k_x}, \tag{2.5}$$

with

$$\boldsymbol{A}_{k_x}(\boldsymbol{U})\hat{\boldsymbol{u}}'_{k_x} = \boldsymbol{P}_L(-\boldsymbol{U} \cdot \nabla_{k_x}\hat{\boldsymbol{u}}'_{k_x} - \hat{\boldsymbol{u}}'_{k_x} \cdot \nabla_{k_x}\boldsymbol{U} + \nu\Delta_{k_x}\hat{\boldsymbol{u}}'_{k_x}), \tag{2.6}$$

and $\boldsymbol{P}_L$ is the Leray projection enforcing non-divergence of the k_x Fourier components of the perturbation velocity field with $\nabla_{k_x} \stackrel{def}{=} (ik_x, \partial_y, \partial_z)$ and $\Delta_{k_x} \stackrel{def}{=} \partial_y^2 + \partial_z^2 - k_x^2$ (Foias *et al.* 2001). The RNL system can then be written in the form:

$$\partial_t \boldsymbol{U} + \boldsymbol{U} \cdot \nabla \boldsymbol{U} - G(t)\hat{\boldsymbol{x}} + \nabla P - \nu\Delta \boldsymbol{U} = -\frac{1}{2}\sum_{k_x \in K_x} \text{Re}[\partial_y(\hat{v}'_{k_x}\hat{\boldsymbol{u}}'^*_{k_x}) + \partial_z(\hat{w}'_{k_x}\hat{\boldsymbol{u}}'^*_{k_x})], \tag{2.7a}$$

$$\partial_t \hat{\boldsymbol{u}}'_{k_x} = \boldsymbol{A}_{k_x}(\boldsymbol{U})\hat{\boldsymbol{u}}'_{k_x}, \quad k_x \in K_x, \tag{2.7b}$$

$$\nabla \cdot \boldsymbol{U} = 0, \quad \nabla_{k_x} \cdot \hat{\boldsymbol{u}}'_{k_x} = 0, \tag{2.7c,d}$$

with $*$ in (2.7a) denoting complex conjugation.

3. DNS and RNL simulations

The data were obtained from a DNS of (2.1) and from an RNL simulation, of (2.3), that is directly associated with the DNS through eliminating the perturbation–perturbation interaction in the perturbation equation. The dynamics were expressed

Abbreviation	$[L_x, L_z]/h$	$N_x \times N_z \times N_y$	Re_τ	$[L_x^+, L_z^+]$
NS940	$[\pi, \pi/2]$	$256 \times 255 \times 385$	939.9	[2953, 1476]
RNL940	$[\pi, \pi/2]$	$256 \times 255 \times 385$	882.4	[2772, 1386]
RNL940k_x12	$[\pi, \pi/2]$	$3 \times 255 \times 385$	970.2	[3048, 1524]

TABLE 1. Simulation parameters. $[L_x, L_z]/h$ is the domain size in the streamwise and spanwise direction. N_x, N_z are the number of Fourier components after dealiasing and N_y is the number of Chebyshev components. Re_τ is the Reynolds number of the simulation based on the friction velocity and $[L_x^+, L_z^+]$ is the channel size in wall units. The Reynolds number based on the bulk velocity is $Re = U_b h/\nu = 18511$ in all cases.

in the form of evolution equations for the wall-normal vorticity and the Laplacian of the wall-normal velocity, with spatial discretization and Fourier dealiasing in the two wall-parallel directions and Chebyshev polynomials in the wall-normal direction (Kim *et al.* 1987). Time stepping was implemented using the third-order semi-implicit Runge–Kutta method.

The geometry and resolution of the DNS and RNL simulations is given in table 1.

Quantities reported in outer units have lengths scaled by the channel half-width, h, and time by h/u_τ and the corresponding Reynolds number is $Re_\tau = u_\tau h/\nu$ where $u_\tau = \sqrt{\nu \, dU/dy|_w}$ (with $dU/dy|_w$ being the shear at the wall) is the friction velocity. Quantities reported in inner units have lengths scaled by $h_\tau = Re_\tau^{-1} h$ and time by $Re_\tau^{-1} h/u_\tau$. Velocities scaled by the friction velocity u_τ will be denoted with the superscript $+$, which indicates inner unit scaling.

We report results from three simulations: a DNS simulation, denoted NS940, with $Re_\tau \approx 940$, the corresponding RNL simulation, denoted RNL940, and a constrained RNL simulation, denoted RNL940k_x12. Both RNL simulations were initialized with an NS940 state and run until a steady state was established. In RNL940k_x12, only the single streamwise Fourier component with wavenumber $k_x h = 12$ was retained in (2.7*b*) by limiting the spectral components of the perturbation equation to only this streamwise wavenumber; this simulation self-sustained a turbulent state with $Re_\tau = 970.2$. In RNL940, the number of streamwise Fourier components was not constrained; this simulation self-sustained a turbulent state at $Re_\tau = 882.2$.

We show in figure 2 the transition from NS940 to RNL940 turbulence. The NS940 is switched at time $tu_\tau/h = 100$ to an RNL simulation by suppressing the perturbation–perturbation interactions, represented by the right-hand side in (2.1*b*). The transition from DNS to RNL is evident in the time series of the energy density of the streamwise Fourier components of the perturbation field, given by:

$$E_{k_x} = \frac{1}{4h} \int_0^h dy [|\hat{\boldsymbol{u}}'_{k_x}|^2]_z. \tag{3.1}$$

The time evolution of the energy density of the first 15 streamwise Fourier components, with wavenumbers $hk_x = 2, 4, \ldots, 30$, in NS940 and in RNL940 is shown in figure 2(*a*). In NS940, all k_x components maintain non-zero energy density. After the transition, the RNL940 turbulence is maintained by interaction between the set of six surviving wavenumbers, $hk_x = 2, 4, \ldots, 12$ and the $k_x = 0$ Fourier component of the flow (cf. figure 2*a*). The result of restriction of NS dynamics to RNL is a spontaneous reduction in the support of the turbulence in streamwise Fourier components, with all Fourier components having wavelength smaller than
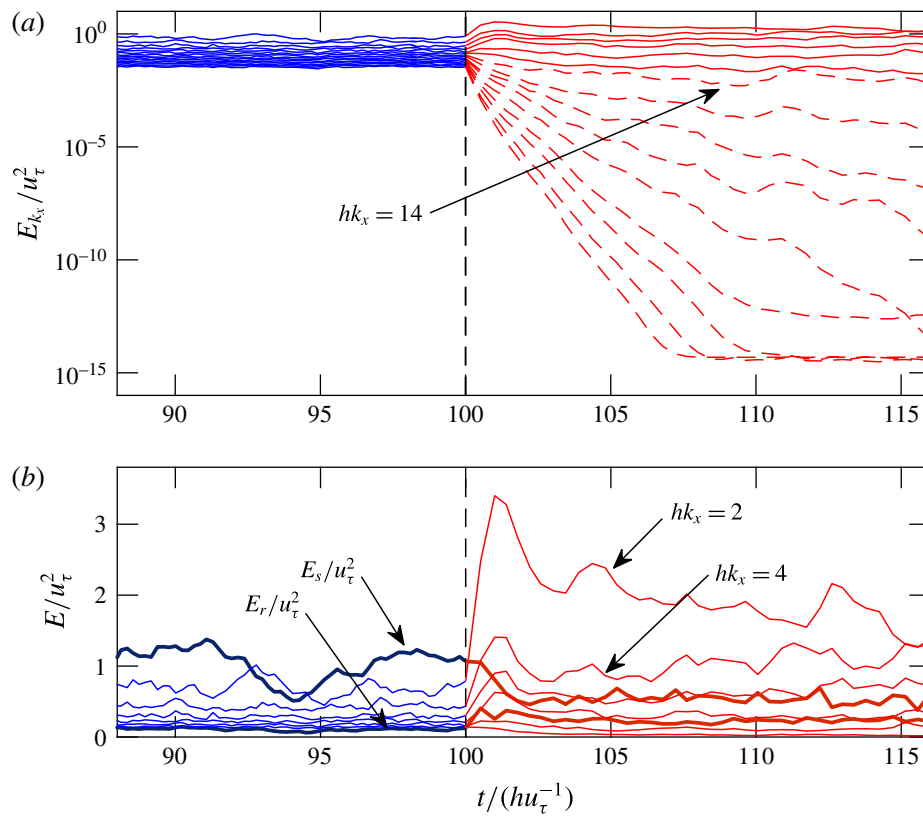
FIGURE 2. (Colour online) An NS940 simulation up to $t/(hu_\tau^{-1}) = 100$ (indicated with the vertical line) is continued subsequently under RNL dynamics. (*a*) The energy density, E_{k_x}, of the first 15 streamwise-varying Fourier components ($hk_x = 2, 4, \ldots, 30$). The energy density of the Fourier components decreases monotonically with increasing wavenumber. Decaying Fourier components are indicated with dashed lines. After the transition to RNL dynamics, all components with $hk_x \geqslant 14$ decay ($hk_x = 14$ decays, although it is not apparent until later times than shown in this figure). Asymptotically the dynamics of the RNL940 turbulence is maintained by interaction between the set of surviving $hk_x = 2, 4, \ldots, 12$ Fourier components and the mean flow ($k_x = 0$). (*b*) Detailed view showing the energy density of the mean and surviving perturbation components during the transition from NS to RNL dynamics, in which the total energy increased by 10 %. For the $k_x = 0$ shown are: the streak energy density, E_s, and roll energy density, E_r. The energy density of the $hk_x = 2, 4, 6, 8$ components increases rapidly during the adjustment after transition to RNL dynamics. Note that the total energy density in the perturbation $k_x \neq 0$ components decreases from $0.91u_\tau^2$ in the NS940 ($0.56u_\tau^2$ being in the components that survive in the RNL) to $0.78u_\tau^2$ in RNL940. Also the roll/streak energy density decreases from $1.1u_\tau^2$ in NS940 to $0.8u_\tau^2$ in RNL940, while the energy density of the $k_x = k_z = 0$ component increases from $397u_\tau^2$ to $448u_\tau^2$.

$\pi h/6$ ($hk_x > 12$) decaying exponentially, producing a reduced complexity dynamics in which turbulence self-sustains on this greatly restricted support in streamwise Fourier components. We view this transition of NS940 turbulence to RNL940 turbulence as revealing the set of structures that are naturally involved in maintaining the turbulent state. Given this spontaneous complexity reduction, the question arises: how few streamwise-varying perturbation components are required in order to self-sustain RNL turbulence at this Reynolds number? We show in RNL940k_x12 that, even if we retain only the single perturbation component with wavelength $\pi h/6$ ($hk_x = 12$), a realistic

self-sustained turbulent state persists. (For a discussion of the streamwise wavenumber support of RNL turbulence cf. Thomas *et al.* 2015.)

4. RNL as a minimal turbulence model

We have seen that as a result of its dynamical restriction, RNL turbulence with the stochastic parameterization set to zero is supported by a small subset of streamwise Fourier components. In order to understand this property of RNL dynamics, consider that the time-dependent streamwise mean state of a turbulent RNL simulation has been stored, so that the mean flow field $\boldsymbol{U}(y, z, t)$ is known at each instant. Then each k_x component of the perturbation flow field that is retained in the RNL evolves according to (2.7b):

$$\partial_t \hat{\boldsymbol{u}}'_{k_x} = \boldsymbol{A}_{k_x}(\boldsymbol{U}) \hat{\boldsymbol{u}}'_{k_x}, \tag{4.1}$$

with $\boldsymbol{A}_{k_x}(\boldsymbol{U})$ given by (2.6).

With the time-dependent mean flow velocity $\boldsymbol{U}$ obtained from a simulation of a turbulent state imposed, equations (4.1) are time-dependent linear equations for $\hat{\boldsymbol{u}}'_{k_x}$ with the property that each k_x streamwise component of the perturbation state of the RNL, $\hat{\boldsymbol{u}}'_{k_x}$, can be recovered with exponential accuracy (within an amplitude factor and a phase) by integrating forward (4.1) regardless of the initial state. This follows from the fundamental property of time-dependent systems that all initial states, $\hat{\boldsymbol{u}}'_{k_x}$ $(y, z, t = 0)$, converge eventually with exponential accuracy to the same structure (for a proof cf. Farrell & Ioannou 1996b). This is completely analogous to the familiar result that regardless of the initial perturbation (with measure zero exception) an autonomous linear system converges to a rank-one structure as time increases: the eigenvector of maximum growth. In fact, each of the $\hat{\boldsymbol{u}}'_{k_x}$ assumes the unique structure of the top Lyapunov vector associated with the maximum Lyapunov exponent of (4.1) at wavenumber k_x, which can be obtained by calculating the limit:

$$\lambda_{k_x} = \limsup_{t \to \infty} \frac{\log \|\hat{\boldsymbol{u}}'_{k_x}(y, z, t)\|}{t}, \tag{4.2}$$

where $\|\cdot\|$ is any norm of the velocity field. Moreover, for each k_x, this top Lyapunov exponent has the further property of being either exactly zero or negative, with those structures having $\lambda_{k_x} = 0$ supporting the perturbation variance. The vanishing of the maximum Lyapunov exponents of linear equations (4.1) reflects the property that the perturbation k_x components that are self-sustained in the turbulent state neither decay to zero nor grow without bound.

This property of RNL turbulence being sustained by the top Lyapunov perturbation structures implies that the perturbation structure contains only the streamwise-varying perturbation Fourier components, k_x, that are contained in the support of these top Lyapunov structures with $\lambda_{k_x} = 0$. It is remarkable that only six Fourier components, k_x, are contained in the support of RNL940, and even more remarkable that the RNL SSP persists even when this naturally reduced set is further truncated to a single streamwise Fourier component, as demonstrated in RNL940k_x12. This result was first obtained in the case of self-sustained Couette turbulence at low Reynolds numbers (cf. Farrell & Ioannou 2012; Thomas *et al.* 2014).

This vanishing of the Lyapunov exponent associated with each streamwise wavenumber is enforced in RNL by the nonlinear feedback process acting between the streaks and the perturbations, by which the parametric instability of the perturbations is suppressed at sufficiently high streak amplitude so that the instability in the asymptotic limit maintains zero Lyapunov exponent (Farrell & Ioannou 2012, 2016).
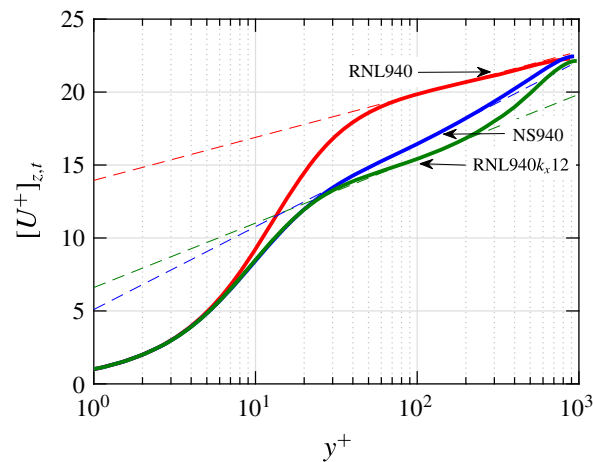
FIGURE 3. (Colour online) Streamwise velocity $[U^+]_{z,t}$ for the simulations listed in table 1. The dashed lines indicate the best fit to the law of the wall, $[U^+(y)]_{z,t} = (1/\kappa) \log(y^+) + C$, with coefficients: $\kappa = 0.40$, $C = 5.1$ for NS940, $\kappa = 0.77$, $C = 14.0$ for RNL940 and $\kappa = 0.53$, $C = 6.6$ for RNL940k_x12.

5. Comparison between NS and RNL turbulence structure and dynamics

In this section we compare turbulence diagnostics obtained from self-sustaining turbulence in the RNL system (2.3), to diagnostics obtained from a parallel associated DNS of (2.1) (cf. table 1 for the parameters). The corresponding turbulent mean profiles for the NS940, RNL940 and RNL940k_x12 simulations are shown in figure 3.

Previous simulations in Couette turbulence at lower Reynolds numbers ($Re_\tau = 65$) showed very small difference between the mean turbulent profile in NS and RNL simulations (Thomas *et al.* 2014). These simulations at larger Reynolds numbers show significant differences in the mean turbulent profiles sustained by NS940 and RNL940 simulations. This is especially pronounced in the outer regions, where RNL940 sustains a mean turbulent profile with substantially smaller shear.

All these examples exhibit a logarithmic layer. However, the shear in these logarithmic regions is different: the von Kármán constant of NS at $Re_\tau = 940$ is $\kappa = 0.4$, while for the RNL940 it is $\kappa = 0.77$ and for the RNL940k_x12 it is $\kappa = 0.53$. Formation of a logarithmic layer indicates that the underlying dynamics of the logarithmic layer are retained in RNL. Because in the logarithmic layer RNL dynamics maintains in local balance with dissipation essentially the same stress and variance as NS, but with a smaller shear, RNL dynamics is in this sense more efficient than NS in that it produces the same local Reynolds stress while requiring less local energy input to the turbulence. To see this, consider that local energy balance in the log-layer requires that the energy production, $U'u_\tau^2$ (with $U' \stackrel{def}{=} \mathrm{d}[U]_{z,t}/\mathrm{d}y$), equals the energy dissipation ϵ, and, because in the log-layer $U' = u_\tau/(\kappa y)$, local balance requires that $u_\tau^3/(\kappa y) = \epsilon$, as discussed by Townsend (1976) and Dallas, Vassilicos & Hewitt (2009). This indicates that the higher κ in RNL simulations with the same u_τ is associated with smaller dissipation than in the corresponding DNS. In RNL dynamics this local equilibrium determining the shear, and by implication κ, results from establishment of a statistical equilibrium by the feedback between the perturbation equation and the mean flow equation, with this feedback producing a κ determined to maintain energy balance locally in y. These considerations imply that the κ observed produces a local shear for which, given the turbulence structure
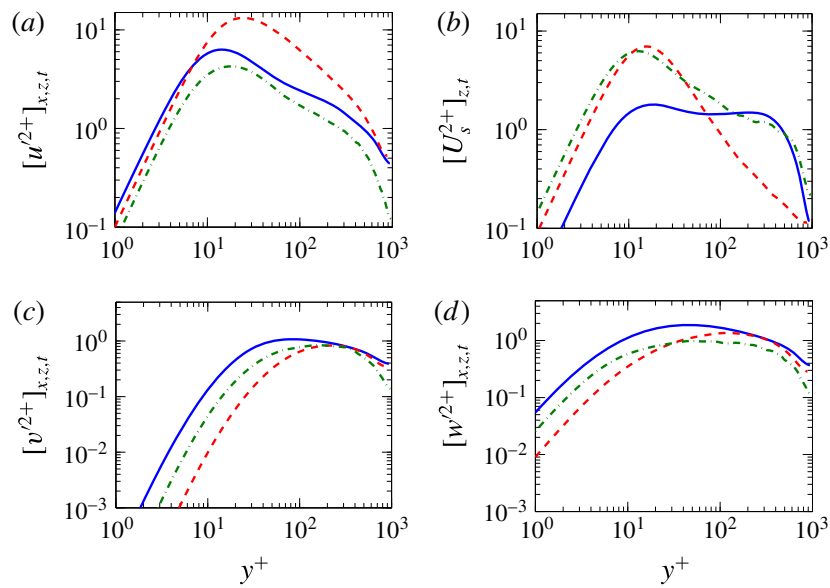
FIGURE 4. (Colour online) Comparison of velocity fluctuations for the simulations listed in table 1. Shown are (*a*) $[u'^{2+}]_{x,z,t}$, (*b*) $[U_s^{2+}]_{z,t}$, (*c*) $[v'^{2+}]_{x,z,t}$, (*d*) $[w'^{2+}]_{x,z,t}$ for NS940 (solid), RNL940 (dashed) and RNL940k_x12 (dash-dot).

produced by the restricted set of retained Fourier components in RNL, the Reynolds stress and dissipation are in local balance. Examination of the transition from NS940 to RNL940, shown by the simulation diagnostics in figure 2(*b*), reveals the action of this feedback control associated with the reduction in shear of the mean flow. When in (2.1*b*) the interaction among the perturbations is switched off, so that the simulation is governed by RNL dynamics, an adjustment occurs in which the energy of the surviving $k_x \neq 0$ components obtain new statistical equilibrium values. An initial increase of the energy of these components is expected because the dissipative effect of the perturbation–perturbation nonlinearity that acts on these components is removed in RNL. As these modes grow, the SSP cycle adjusts to establish a new turbulent equilibrium state which is characterized by increase in energy of the largest streamwise scales and on average a reduction in streak amplitude. In the outer layer this new equilibrium is characterized in the case of RNL940 by reduction of the shear of the mean flow and reduction in the streak amplitude (cf. figure 3).

A comparison of the perturbation statistics of RNL940 with NS940 is shown in figure 4. The u' component of the perturbation velocity fluctuations is significantly more pronounced in RNL940 (cf. figure 4*a*) and the magnitude of the streak in RNL940 exceeds significantly the streak magnitude in NS940 in the inner-wall region (cf. figure 4*b*). In contrast, the wall-normal and spanwise fluctuations in RNL940 are less pronounced than in NS940 (cf. figure 4*c*,*d*) and the streak fluctuations in the outer region are also less pronounced in RNL940 (cf. figure 4*b*).

Despite these differences in the r.m.s. values of the velocity fluctuations, both RNL940 and NS940 produce very similar Reynolds stress $-[uv]_{x,z,t}$ which is the sum of $-[U_sV]_{z,t}$ and $-[u'v']_{x,z,t}$. Comparison of the wall-normal distribution of these two components of the Reynolds stress is shown in figure 5(*a*). Because the turbulence in NS940 and RNL940 is sustained with essentially the same pressure gradient, the sum of these Reynolds stresses is the same linear function of *y* outside the viscous layer. The Reynolds stress is dominated by the perturbation Reynolds stress $-[u'v']_{x,z,t}$ in all
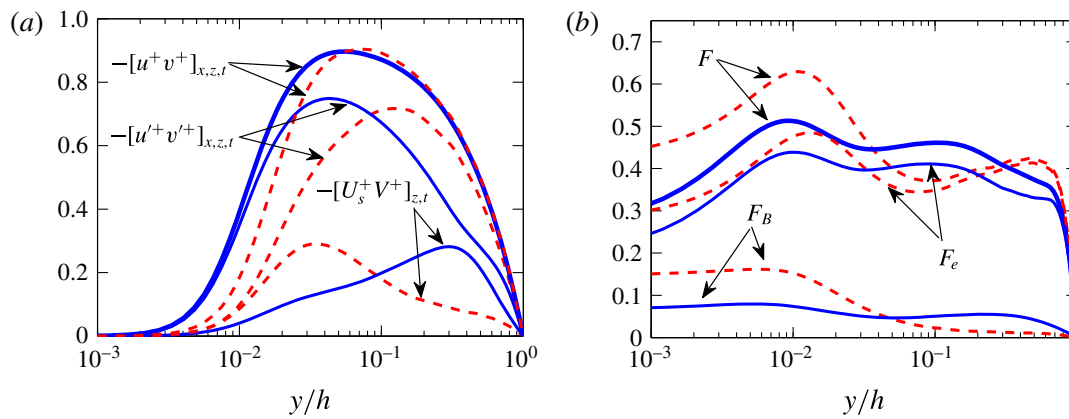
FIGURE 5. (Colour online) (*a*) The Reynolds stress component, $-[uv]_{x,z,t}$ in NS940 (solid) and in RNL940 (dashed). Also shown are each of the terms, $-[U_s V]_{z,t}$ and $-[u'v']_{x,z,t}$ that sum to $-[uv]_{x,z,t}$. Although the NS and RNL values of the total $-[uv]_{x,z,t}$ are almost identical, the contribution of $-[U_s V]_{z,t}$ and $-[u'v']_{x,z,t}$ differ in NS and RNL. (*b*) Structure coefficient, F, in NS940 (solid) and in RNL940 (dashed). Shown are $F_B = -[UV]_{z,t}/\sqrt{[U^2]_{z,t}[V^2]_{z,t}}$, $F_e = -[u'v']_{x,z,t}/\sqrt{[u'^2]_{x,z,t}[v'^2]_{x,z,t}}$ and $F = -[uv]_{x,z,t}/\sqrt{[u^2]_{x,z,t}[v^2]_{x,z,t}}$.
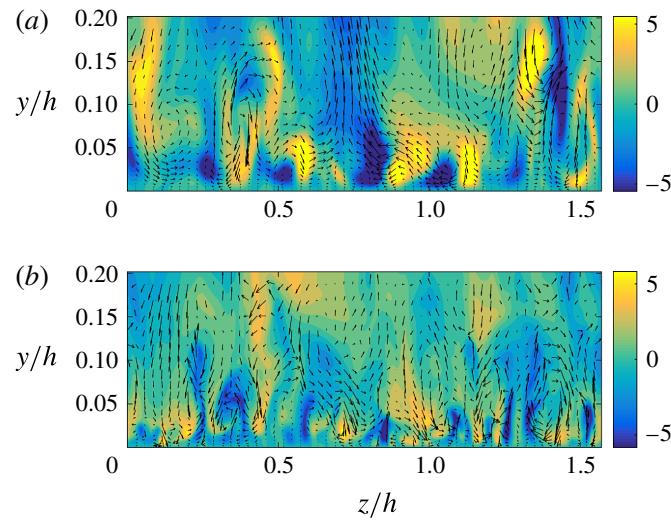

FIGURE 6. (Colour online) Perturbation structure, $\boldsymbol{u}'^+$ in (y, z)-plane cross-section for (*a*) RNL940 and (*b*) NS940 in the inner-wall region, $0 \leqslant y/h \leqslant 0.2$. Both panels show a colour mapping of the u'^+ field, superimposed with (v'^+, w'^+) velocity vectors.

simulations, with the RNL stress penetrating farther from the wall. This is consistent with the fact that the perturbation structure in RNL has larger scale. This can be seen in a comparison of the NS and RNL perturbation structure shown in figure 6. Note that the Reynolds stress $-[U_s V]_{z,t}$ associated with the streak and roll in the outer region of the NS940 simulation is larger than that in RNL940. Further, the average correlation between the perturbation u' and v' fields are almost the same in both simulations, while the correlation between the U_s and V in RNL940 is much smaller than that in NS940 in the outer layer. This is seen in a plot of the structure coefficient (cf. Flores & Jiménez 2006) shown in figure 5(*b*).
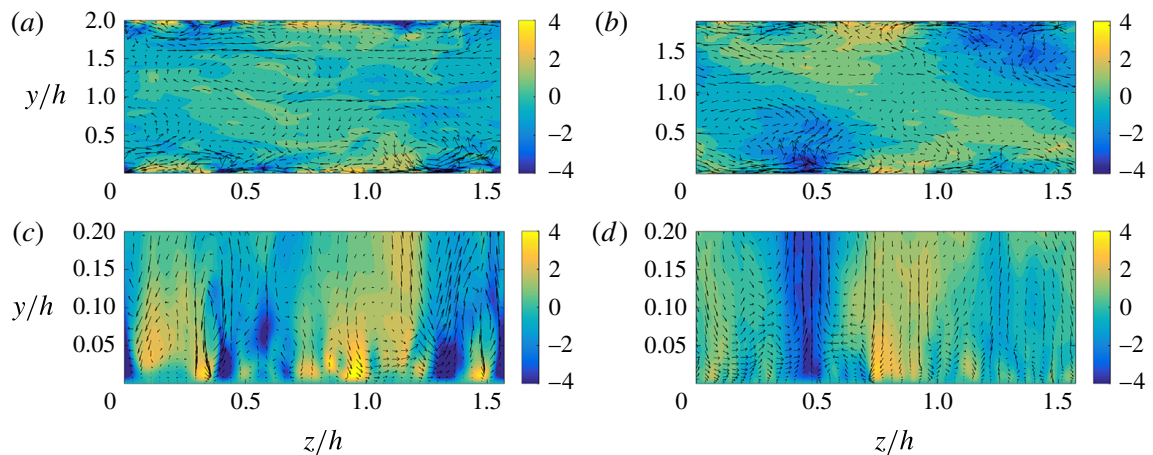
FIGURE 7. (Colour online) Instantaneous streak component of the flow, U_s^+, shown as a (y, z)-plane cross-section for (a,c) RNL940 and (b,d) NS940. All panels show a colour mapping of the streak velocity, U_s^+, superimposed with (V^+, W^+) velocity vectors. Panels (a) and (b) show the whole channel while panels (c) and (d) show the inner-wall region, $0 \leqslant y/h \leqslant 0.2$.

Turning now to the flow structures in the NS940 and RNL940 simulations, a (y, z)-plane snapshot of the streamwise mean flow component (corresponding to $k_x = 0$ streamwise wavenumber) is shown in figure 7. A colour mapping of the streamwise streak component, U_s, is shown together with vectors of the streamwise mean (V, W) field, which indicates the velocity components of the large-scale roll structure. The presence of organized streaks and associated rolls is evident both in the inner-wall and in the outer-wall region. Note that, in comparison with the streak in NS940, the streak in RNL940 has a finer (y, z) structure, which is consistent with the energy of the streak being more strongly dissipated by diffusion in RNL (cf. figure 7). A three-dimensional perspective of the flow in NS940 and RNL940 is shown in figure 8. Note that in RNL940 there is no visual evidence of the $k_x = 0$ roll/streak structure which is required by the restriction of RNL dynamics to be the primary structure responsible for organizing and maintaining the self-sustained turbulent state. Rather, the most energetic structure among the perturbations maintaining the pivotal streamwise mean roll/streak is the structure that dominates the observed turbulent state. We interpret this as indicating that the $k_x = 0$ roll/streak structure, which is the dynamically central organizing structure in RNL turbulence and which organizes the turbulence on scale unbounded in the streamwise direction, cannot be reliably identified by visual inspection of the flow fields, which would lead one to conclude that the organizing scale was not just finite but the rather short scale of the separation between perturbations to the streak. Essentially this same argument is cast in terms of the inability of Fourier analysis to identify the organization scale of the roll/streak structure by Hutchins & Marusic (2007). This dynamically central structure, which appears necessarily at $k_x = 0$ in RNL dynamics, is reflected in the highly streamwise elongated structures seen in simulations and observations of DNS wall turbulence. While in a long channel averaging would be expected to suppress the $k_x = 0$ component in DNS, in the short channel used here, the $k_x = 0$ component is prominent in both the RNL940 and NS940 (cf. figure 7).

An alternative view of turbulence structure is provided by comparison of the spectral energy densities of velocity fields as a function of streamwise and spanwise wavenumber, (k_x, k_z). The pre-multiplied spectral energy densities of each of the
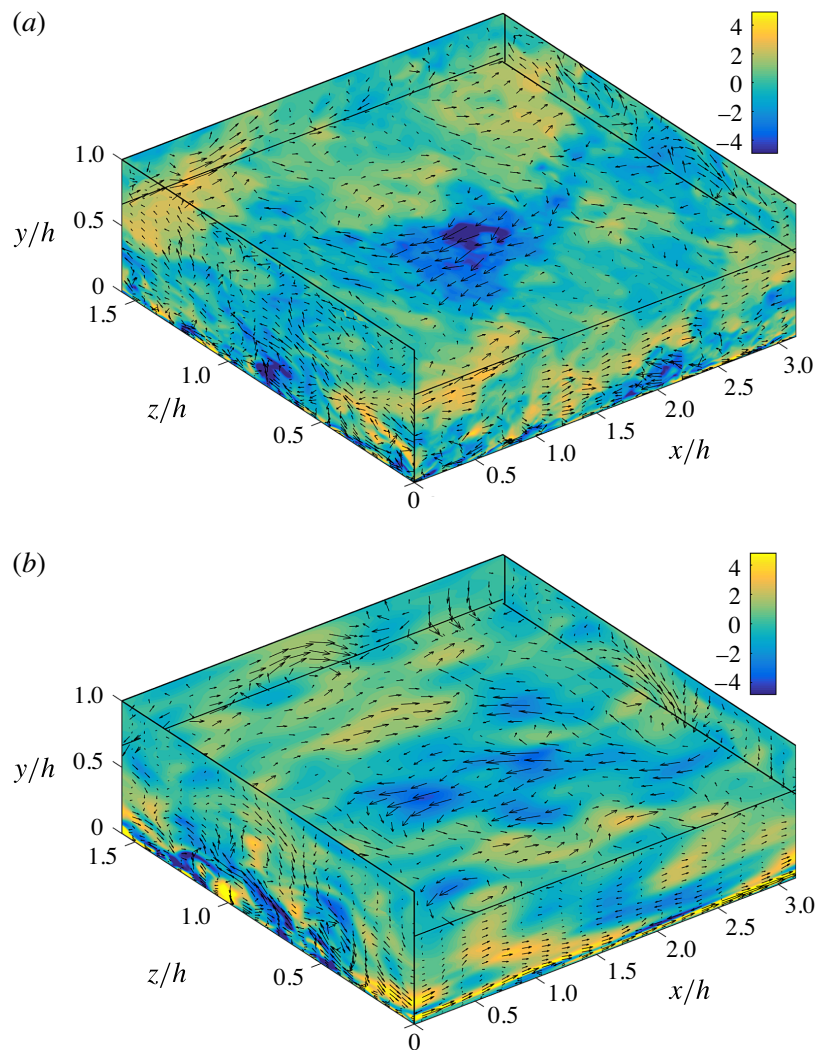
FIGURE 8. (Colour online) Three-dimensional perspective plots of the flow at a single time for (*a*) NS940 and (*b*) RNL940, for the lower half of the channel, $0 \leqslant y/h \leqslant 1$. Both images show a colour mapping of the streak component plus streamwise perturbation, $U_s^+ + u'^+$. The central *x*–*z* panel shows the flow at channel height, $y/h = 0.65$. The superimposed vectors represent the $(U_s^+ + u'^+, w^+)$ velocities for the (x, z)-plane, $(U_s^+ + u'^+, v^+)$ velocities for the (x, y)-plane and (v^+, w^+) velocities for the (y, z)-plane. The parameters of the simulations are given in table 1.

three components of velocity, E_{uu}, E_{vv} and E_{ww}, are shown at heights $y^+ = 20$, representative of the inner-wall region; and at $y/h = 0.65$, representative of the outer-wall region, in figure 9. While RNL940 produces spanwise streak spacing and rolls similar to those in NS940, the tendency of RNL to produce longer structures in this diagnostic is also evident. The spectra for the outer region indicate similar large-scale structure and good agreement in the spanwise spacing between RNL940 and NS940. This figure establishes the presence of large-scale structure in the outer region in both RNL940 and NS940. It has been noted that in NS940, while the scale of the structures increases linearly with distance from the wall in the inner-wall region, in the outer regions the structures having the largest possible streamwise scale dominate the flow variance at high Reynolds number (Jiménez 1998; Jiménez & Hoyas 2008). This linear scaling near the wall can also be seen in figure 10, where
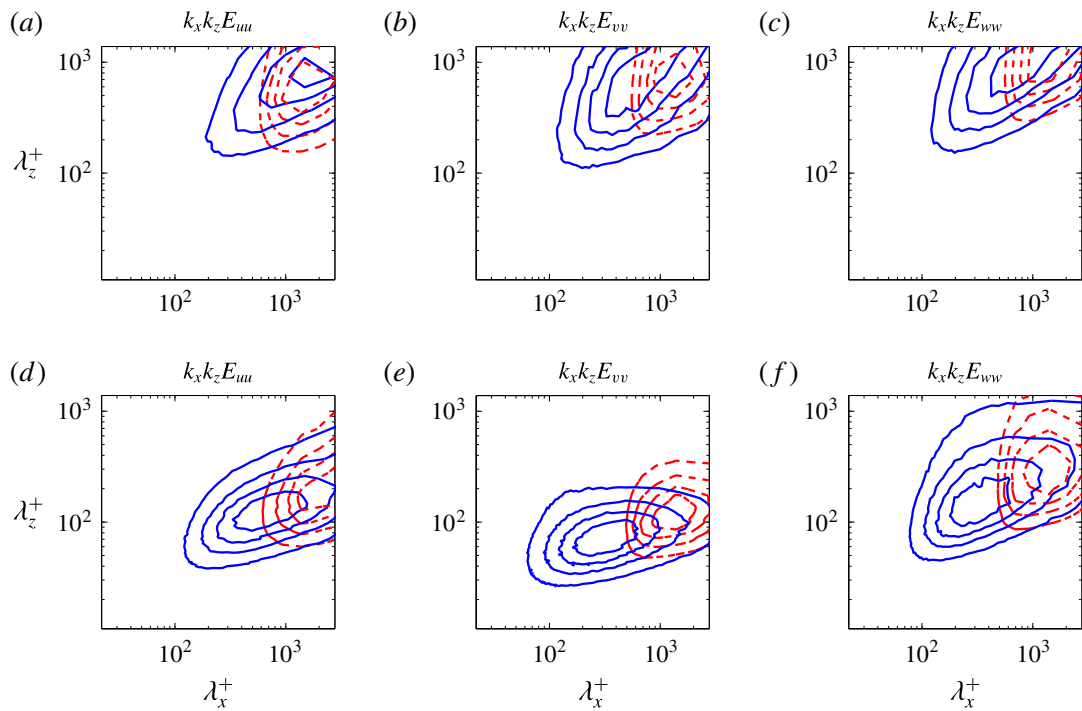
FIGURE 9. (Colour online) Contours of pre-multiplied power spectra $k_x k_z E_{ff}(k_x, k_z)$ with $f = u, v, w$, as a function of λ_x^+ and λ_z^+ for NS940 (solid) and RNL940 (dashed). (*a–c*) Show the spectral energy densities at wall distance $y/h = 0.65$ for u, v and w, respectively, while (*d–f*) show the corresponding spectral energy densities at $y^+ = 20$. Contours are (0.2, 0.4, 0.6, 0.8) times the maximum value of the corresponding spectrum. The maximum λ_x^+ and λ_y^+ are the lengths L_x^+ and L_z^+ of the periodic channel.

contour plots of normalized pre-multiplied one-dimensional spectral energy densities as a function of spanwise wavelength, k_z, and wall-normal distance, as in Jiménez (1998) and Jiménez & Hoyas (2008), are shown for NS940 and RNL940. In both simulations, the spanwise wavelength associated with the spectral density maxima increases linearly with wall distance, with this linear dependence being interrupted at $y/h \approx 0.5$ (or $y^+ \approx 450$). Beyond $y/h \approx 0.5$, structures assume the largest λ_z allowed in the channel, suggesting simulations be performed in larger boxes in future work (cf. discussion by Jiménez & Hoyas (2008) and Flores & Jiménez (2010)). Corresponding contour plots of spectral energy density as a function of streamwise wavelength and wall-normal distance are shown in figure 11. These plots show that the perturbation variance in the inner-wall and outer-wall region is concentrated in a limited set of streamwise components. In the case of RNL940 the spontaneous restriction on streamwise perturbation wavenumber support that occurs in RNL dynamics produces a corresponding sharp shortwave cutoff in the k_x components of the spectra, as seen in figure 11(*d–f*). Note that the maximum wavelength in these graphs is equal to the streamwise length of the box, and not to the infinite wavelength associated with the energy of the roll/streak structure in RNL dynamics.

6. Streak structure dynamics in NS and RNL dynamics

That RNL dynamics maintains a turbulent state similar to that of NS with nearly the same Re_τ ($Re_\tau = 882$ with the six Fourier components of RNL940 and $Re_\tau = 970.2$ for the single Fourier component with $k_x h = 12$ of RNL940k_x12 versus the $Re_\tau = 940$
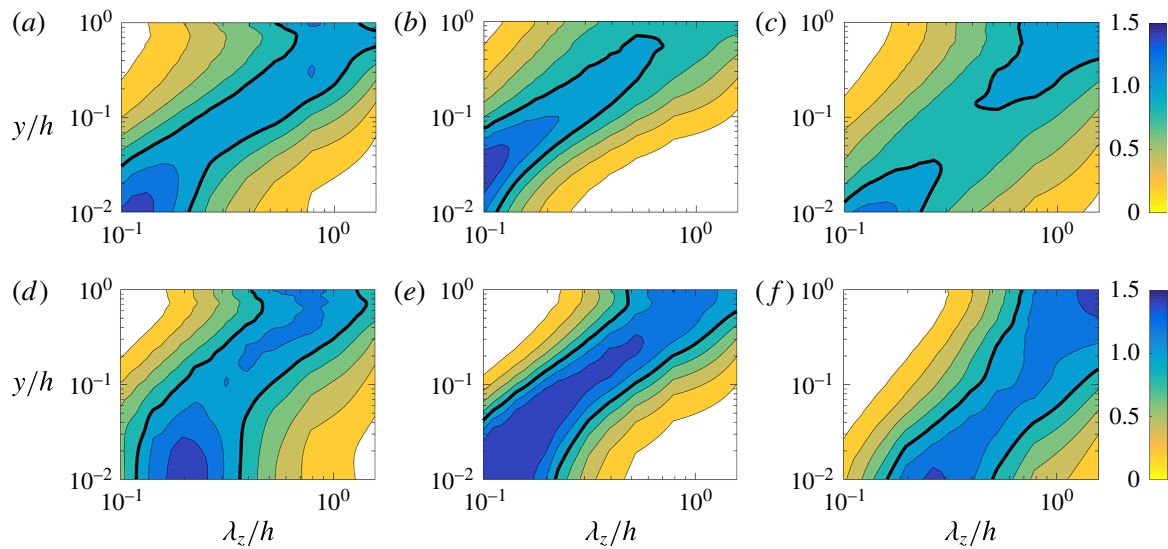
FIGURE 10. (Colour online) Normalized pre-multiplied spectral densities $k_z E_f(k_z) = k_z \sum_{k_x} E_{ff}(k_x, k_z)$, with $f = u, v, w$, as a function of spanwise wavelength, λ_z/h, and y/h. Spectral densities are normalized so that at each y the total energy, $\sum_{k_z} E_f(k_z)$, is the same. (a) $k_z E_u(k_z)$, (b) $k_z E_v(k_z)$, (c) $k_z E_w(k_z)$ for NS940. (d) $k_z E_u(k_z)$, (e) $k_z E_v(k_z)$, (f) $k_z E_w(k_z)$ for RNL940. The isocontours are $0.2, 0.4, \ldots, 1.4$ and the thick line marks the 1.0 isocontour.
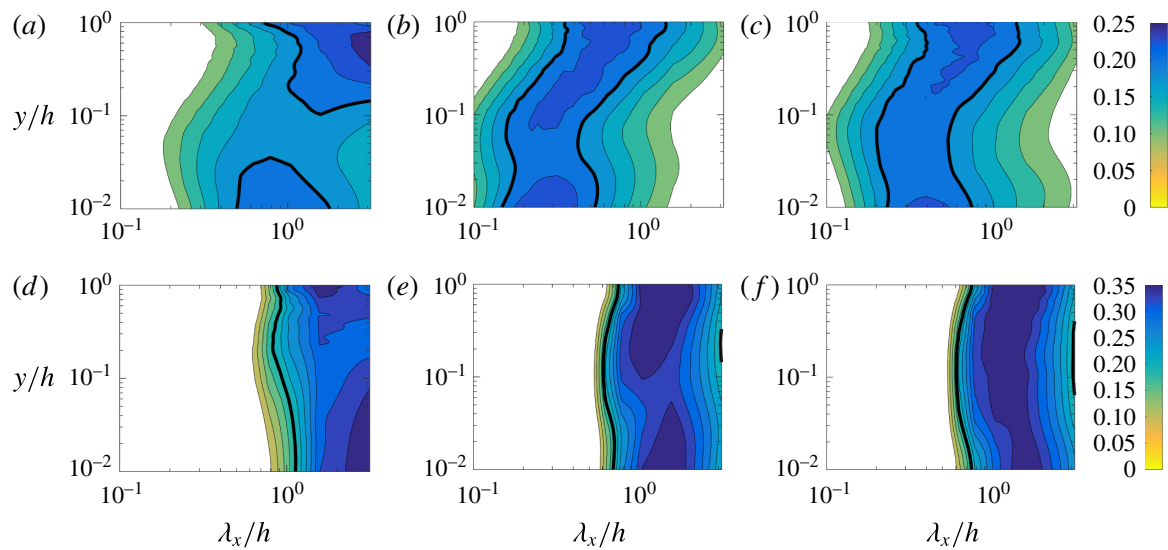

FIGURE 11. (Colour online) Normalized pre-multiplied spectral densities $k_x E_f(k_x) = k_x \sum_{k_z} E_{ff}(k_x, k_z)$, with $f = u, v, w$, as a function of streamwise wavelength, λ_x/h, and y/h. Spectral densities are normalized so that at each y the total energy, $\sum_{k_x} E_f(k_x)$, is the same. (a) $k_x E_u(k_x)$, (b) $k_x E_v(k_x)$, (c) $k_x E_w(k_x)$ for NS940. (d) $k_x E_u(k_x)$, (e) $k_x E_v(k_x)$, (f) $k_x E_w(k_x)$ for RNL940. The isocontours are $0.1, 0.125, \ldots, 0.35$ and the thick line marks the 0.2 isocontour.

of the NS940; cf. table 1) implies that these systems have approximately the same energy production and dissipation, and that the reduced set of Fourier components retained in RNL dynamics assume the burden of accounting for this energy production and dissipation. Specifically, the components in NS940 that are not retained in RNL

dynamics are responsible for approximately one-third of the total energy dissipation, which implies that the components that are retained in RNL940 dynamics must increase their dissipation, and consistently their amplitude, by that much.

Large-scale roll/streak structures are prominent in the inner layer as well as in the outer layer both in NS940 and in RNL940. In the inner layer, the interaction of roll/streak structures with the $k_x \neq 0$ perturbation field maintains turbulence through an SSP (Hamilton *et al.* 1995; Jiménez & Pinelli 1999; Farrell & Ioannou 2012). The RNL system provides an especially simple manifestation of this SSP, as its dynamics comprise only interaction between the mean ($k_x = 0$) and perturbation ($k_x \neq 0$) components. The fact that RNL self-sustains a close counterpart of the NS turbulent state in the inner-wall region provides strong evidence that the RNL SSP captures the essential dynamics of turbulence in this region.

The structure of the RNL system compels the interpretation that the time dependence of the SSP cycle in this system seen in figure 2(b) is an intricate interaction of dynamics among streaks, rolls and perturbations that produces the time-dependent streamwise mean flow $U(y, z, t)$, which, when introduced in (2.7b), results in generation of a particular evolving perturbation Lyapunov structure with exactly zero Lyapunov exponent that simultaneously produces Reynolds stresses contrived to maintain the associated time-dependent mean flow. S3T identifies this exquisitely contrived SSP cycle comprising the generation of the streak through lift-up by the rolls, the maintenance of the rolls by torques induced by the perturbations, which themselves are maintained by time-dependent parametric non-normal interaction with the streak (Farrell & Ioannou 2012).

In RNL this SSP is more efficient than its DNS counterpart in producing downgradient perturbation momentum flux as, with smaller mean shear over most of the channel, a self-sustained turbulence with approximately the same Re_τ as that in NS940 is maintained, as discussed above (cf. § 5). A comparison of the shear, the r.m.s. V velocity, and the r.m.s. streak velocity, U_s, in the outer layer is shown as a function of y in figure 12, from which it can be seen that the ratio of the product of the mean shear and r.m.s. wall-normal velocity to the r.m.s. streak velocity is approximately equal in DNS and in RNL. It is important to note that in the RNL system these dependencies arise due to the feedback control exerted by the perturbation dynamics on the mean flow dynamics by which its statistical steady state is determined. The structure of RNL isolates this feedback control process so that it can be studied, and elucidating its mechanism and properties are the subject of ongoing work.

In the discussion above we have assumed that the presence of roll and streak structure in the log-layer in RNL indicates the existence of an SSP cycle there, and by implication also in NS. In order to examine this SSP, consider the momentum equation for the streamwise streak:

$$\partial_t U_s = \underbrace{-(V\partial_y U - [V\partial_y U]_z) - (W\partial_z U - [W\partial_z U]_z)}_{A}$$
$$\underbrace{-([v'\partial_y u' - [v'\partial_y u']_z]_x) - ([w'\partial_z u' - [w'\partial_z u']_z]_x)}_{B} + \underbrace{\nu\Delta U_s}_{C}. \qquad (6.1)$$

Term A in (6.1) is the contribution to the streak acceleration by the 'lift-up' mechanism and the 'push-over' mechanism, which represent transfer to streak momentum by the mean wall-normal and spanwise velocities, respectively; term B in (6.1) is the contribution to the streak momentum by the perturbation Reynolds stress
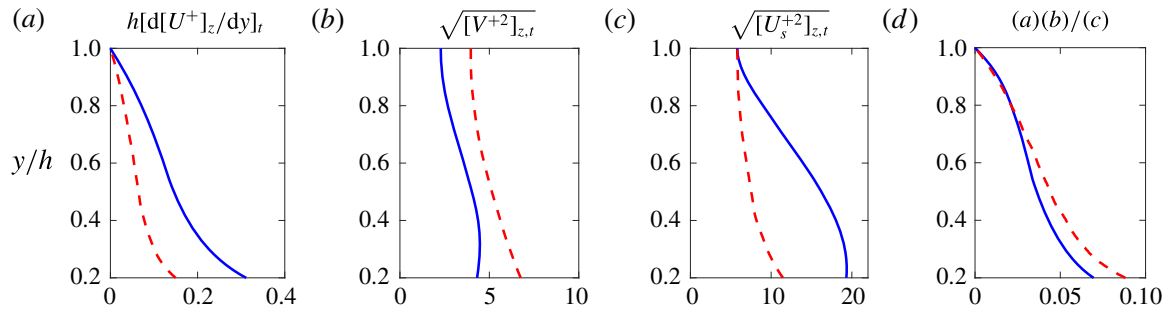
FIGURE 12. (Colour online) Comparison of the (a) turbulent mean shear, $[\mathrm{d}[U^+]_z/\mathrm{d}y]_t h$, (b) the r.m.s. of $[V^+]_z$, (c) the r.m.s. of the streak velocity, U_s^+ and (d) the ratio of the product of the mean shear and r.m.s. wall-normal velocity over the r.m.s. streak velocity, for NS940 (solid) and RNL940 (dashed) in the outer layer, $0.2 \leqslant y/h \leqslant 1$.

divergence (structures with $k_x \neq 0$); term C is the diffusion of the streak momentum due to viscosity.

In order to identify the mechanism of streak maintenance we determine the contribution of terms A–C in (6.1) to the streak momentum budget by evaluating these contributions. The time-averaged results are shown as a function of y over these cross-stream regions of the flow, indicated by R: the whole channel, the outer region, $0.2 \leqslant y/h \leqslant 1.8$, and the inner region, $0 \leqslant y/h < 0.2$ and $1.8 < y/h \leqslant 2$, in figure 13. The contributions are, respectively, the lift-up:

$$I_A(t) = h^{-1} \int_R \mathrm{d}y \mathcal{I}_A(y, t), \quad \text{with } \mathcal{I}_A(y, t) = [\mathrm{sgn}(U_s) \times (\text{Term A})]_z, \quad (6.2)$$

the perturbation Reynolds stress divergence:

$$I_B(t) = h^{-1} \int_R \mathrm{d}y \mathcal{I}_B(y, t), \quad \text{with } \mathcal{I}_B(y, t) = [\mathrm{sgn}(U_s) \times (\text{Term B})]_z, \quad (6.3)$$

and diffusion:

$$I_C(t) = h^{-1} \int_R \mathrm{d}y \mathcal{I}_C(y, t), \quad \text{with } \mathcal{I}_C(y, t) = [\mathrm{sgn}(U_s) \times (\text{Term C})]_z. \quad (6.4)$$

In the inner-wall and outer-wall regions, in both NS940 and RNL940, the streak is maintained only by the lift-up mechanism, while streak momentum is lost on average at all cross-stream levels to both the Reynolds stress divergence and the momentum diffusion. In RNL940 the magnitude of streak acceleration by lift-up is greater than that of NS940 in the inner region, whereas in the outer region the acceleration by lift-up in RNL940 is about half that in NS940, consistent with their similar roll amplitude (cf. figure 12b) and the smaller mean flow shear maintained at statistical steady state in RNL940. In the outer region of the NS940 the Reynolds stress divergence almost completely balances the positive contribution from lift-up, while in RNL940 the lift-up is balanced equally by the Reynolds stress divergence and the diffusion. Enhancement of the contribution by diffusion in the outer layer in RNL940 results from the increase in the spanwise and cross-stream wavenumbers of the streak (cf. figure 7c) resulting from the nonlinear advection of the streak by the V and W velocities. This increase in the spanwise and cross-stream wavenumbers
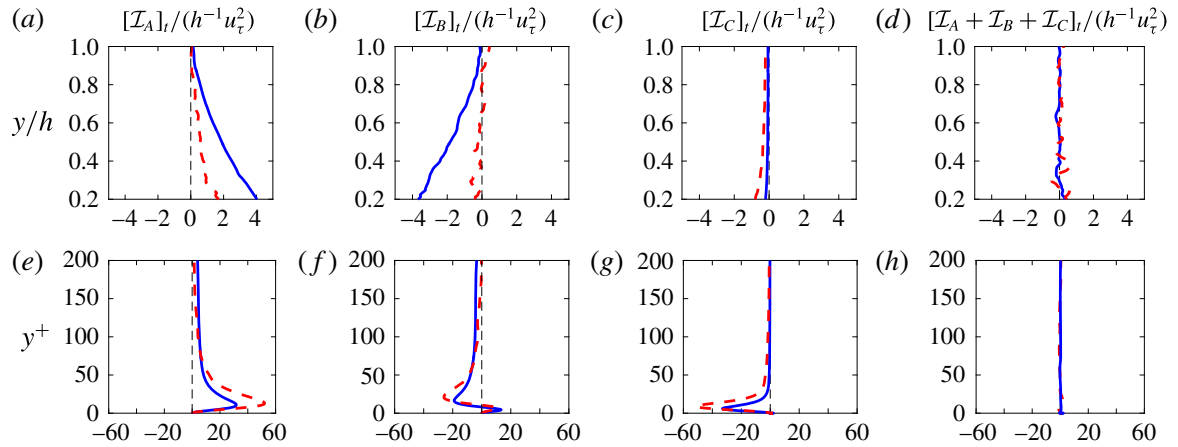
FIGURE 13. (Colour online) Cross-stream structure of the time-averaged contributions to streak acceleration for NS940 (solid) and RNL940 (dashed) from: (a,e) the lift-up mechanism $[\mathcal{I}_A]_t(y)$, (b,f) the perturbation Reynolds stress divergence $[\mathcal{I}_B]_t(y)$ and (c,g) the momentum diffusion $[\mathcal{I}_C]_t(y)$. In (d,h) we plot the sum of these terms which, averaged over a long time interval, should add exactly to zero. $(a$–$d)$ Show structure in the outer layer, $0.2 \leqslant y/h \leqslant 1$, $(e$–$h)$ show the structure in the inner layer, $0 \leqslant y^+ \leqslant 200$.

of the streak in RNL940 due to nonlinear advection by the mean (V, W) roll circulation also implies that the dissipation of streak energy in RNL940 is similarly enhanced. This constitutes an alternative route for energy transfer to the dissipation scale, which continues to be available for establishment of statistical equilibrium in RNL940 despite the limitation in the streamwise wavenumber support inherent in RNL turbulence. The lift-up process is a positive contribution to the maintenance of the streak, and the Reynolds stress divergence is a negative contribution not only in a time-averaged sense, but also at every time instant. This is shown in plots of the time series of the lift-up and Reynolds stress divergence contribution to the streak momentum over the inner region $0 \leqslant y/h < 0.2$ and $1.8 < y/h \leqslant 2$, over the outer region $0.2 \leqslant y/h \leqslant 1.8$, and over the whole channel in figure 14. We conclude that, in both NS940 and RNL940, the sole positive contribution to the outer layer streaks is lift-up, despite the small shear in this region. Consistently, a recent POD analysis in a similar flow setting has confirmed the phase relationship between the streak and wall-normal velocity, indicative of this lift-up mechanism (Nikolaidis *et al.* 2016). We next consider the dynamics maintaining the lift-up.

7. Roll dynamics: maintenance of mean streamwise vorticity in NS and RNL

We have established that the lift-up mechanism is not only responsible for streak maintenance in the inner layer, but also in the outer layer. We now examine the mechanism of the lift-up by relating it to maintenance of the roll structure using as a diagnostic streamwise-averaged vorticity, $\Omega_x = \partial_y W - \partial_z V$. In order for roll circulation to be maintained against dissipation there must be a continuous generation of Ω_x. There are two possibilities for the maintenance of Ω_x in the outer layer: either Ω_x is generated locally in the outer layer, or it is advected from the near-wall region. From (2.1a) we have that Ω_x satisfies the equation:

$$\partial_t \Omega_x = \underbrace{-(V\partial_y + W\partial_z)\Omega_x}_{D} + \underbrace{(\partial_{zz} - \partial_{yy})[v'w']_x - \partial_{yz}([w'^2]_x - [v'^2]_x)}_{F} + \nu\Delta\Omega_x. \qquad (7.1)$$
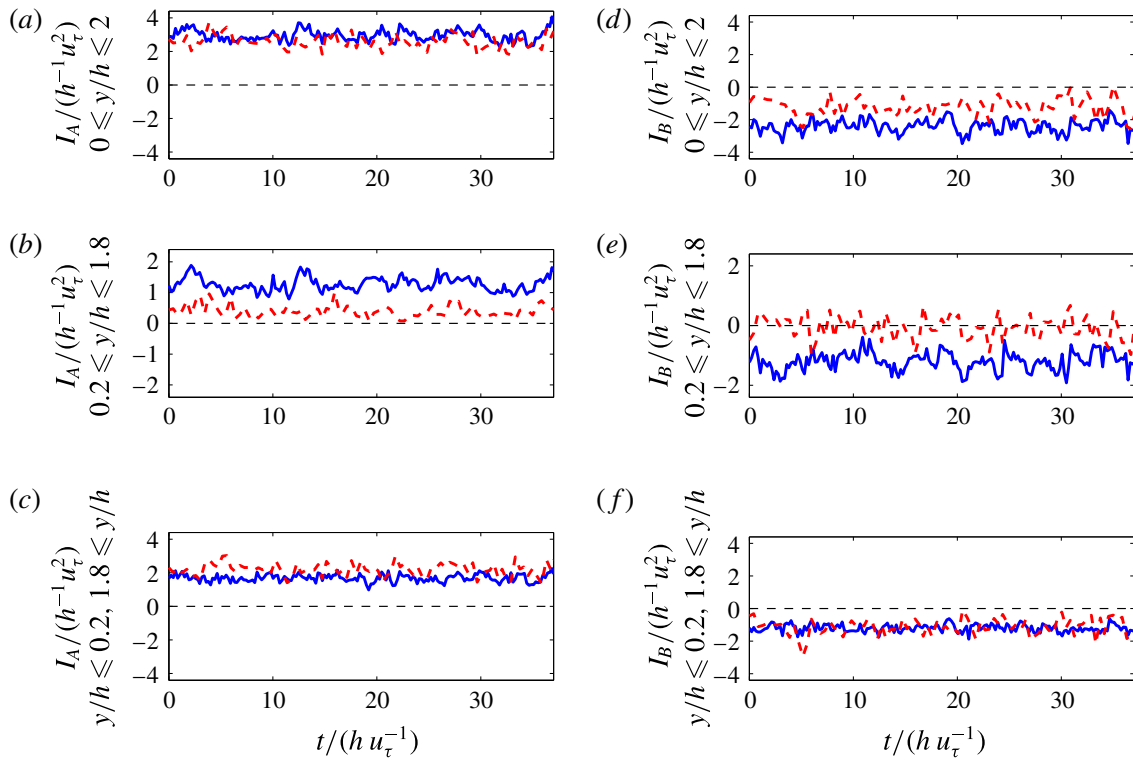
FIGURE 14. (Colour online) Time series of the total $I_A(t)$ (lift-up) for NS940 (solid) and RNL940 (dashed), (*a*) over the whole channel, (*b*) over the outer region, $0.2 \leqslant y/h \leqslant 1.8$, (*c*) over the inner region, $0 \leqslant y/h \leqslant 0.2$ and $1.8 \leqslant y/h \leqslant 2$. Similarly for $I_B(t)$ (Reynolds stress divergence), (*d*) over the whole channel, (*e*) over the outer region, $0.2 \leqslant y/h \leqslant 1.8$, (*f*) over the inner region, $0 \leqslant y/h \leqslant 0.2$ and $1.8 \leqslant y/h \leqslant 2$.

Term D expresses the streamwise vorticity tendency due to advection of Ω_x by the streamwise mean flow (V, W). Because there is no vortex stretching contribution to Ω_x from the (V, W) velocity field, this term only advects the Ω_x field and cannot sustain it against dissipation. However, this term may be responsible for systematic advection of Ω_x from the inner to the outer layer. Term F is the torque induced by the perturbation field. This is the only term that can maintain Ω_x. The overall budget for square streamwise vorticity in the region R, $y_1 \leqslant y \leqslant y_2$, $0 \leqslant z \leqslant L_z$, is given by:

$$\partial_t \int_{y_1}^{y_2} \mathrm{d}y \frac{1}{2}[\Omega_x^2]_z = \underbrace{-\frac{1}{2}[\Omega_x^2 V]_z\big|_{y=y_1}^{y_2}}_{=hI_D} + \underbrace{\int_{y_1}^{y_2} \mathrm{d}y[\Omega_x \times \text{Term F}]_z}_{=hI_F} + \nu \int_{y_1}^{y_2} \mathrm{d}y[\Omega_x \Delta \Omega_x]_z,$$
(7.2)

where:

$$I_D(t) = h^{-1} \int_R \mathrm{d}y \mathcal{I}_D(y, t), \quad \text{with } \mathcal{I}_D(y, t) = [\Omega_x \times (\text{Term D})]_z \qquad (7.3)$$

is the advection into cross-stream region, R, and

$$I_F(t) = h^{-1} \int_R \mathrm{d}y \mathcal{I}_F(y, t), \quad \text{with } \mathcal{I}_F(y, t) = [\Omega_x \times (\text{Term F})]_z \qquad (7.4)$$
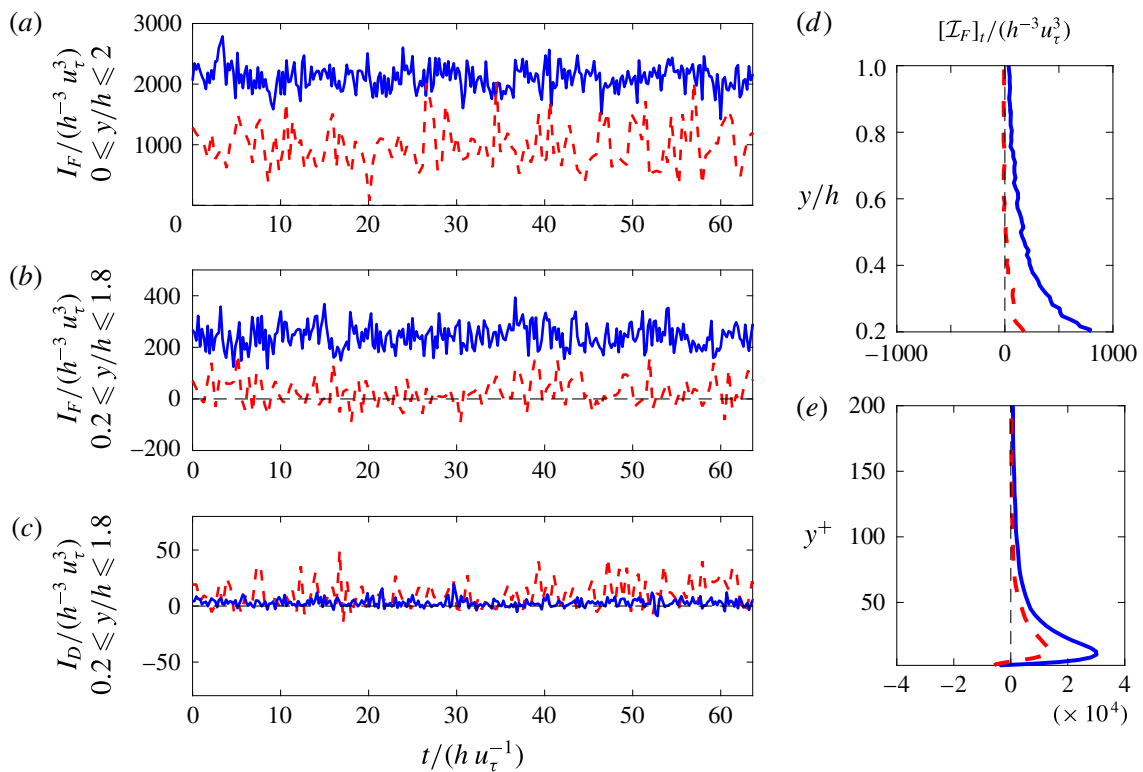
is the Reynolds stress torque production in region R.

FIGURE 15. (Colour online) (*a–c*) Time series of the contribution to the time rate of change of streamwise square vorticity $\int dy[\Omega_x^2/2]_z$ by perturbation torques, I_F, and by advection of streamwise mean vorticity by the mean flow, I_D, for NS940 (solid) and RNL940 (dashed). (*a*) I_F over the whole channel, $0 \leqslant y/h \leqslant 2$ ($I_D = 0$ in this case). The time mean I_F is $2103.6h^{-3}u_\tau^3$ for NS940 and $982.8u_\tau^3$ for RNL940. (*b*) I_F over the outer layer, $0.2 \leqslant y/h \leqslant 1.8$. The time mean I_F for this region is $242.5h^{-3}u_\tau^3$ for NS940 and only $28.7h^{-3}u_\tau^3$ for RNL940. (*c*) I_D for the outer layer $0.2 \leqslant y/h \leqslant 1.8$. The time mean I_D is $2.9h^{-3}u_\tau^3$ for NS940 and $11.2h^{-3}u_\tau^3$ for RNL940. These figures show that in NS940 and RNL940 the roll is maintained locally by the perturbation Reynolds stresses. (*d,e*) Cross-stream structure of the time-averaged contribution to the streamwise mean vorticity generation from perturbation Reynolds-stress-induced torques $[\mathcal{I}_F]_t(y)$.

Time series of the contributions from $I_D(t)$ and $I_F(t)$ to the Ω_x production for NS940 and RNL940, shown in figure 15(*a–c*), demonstrate that Ω_x is primarily generated *in situ* by Reynolds stress torques. The corresponding wall-normal structure of the time mean of $\mathcal{I}_F$, representing the local contribution to streamwise mean vorticity generation from perturbation Reynolds-stress-induced torques, is shown in figure 15(*d,e*). Note that for NS940 in the outer layer the streamwise mean vorticity generation by the Reynolds stress is strongly positive at each instant. This implies a systematic positive correlation between the roll circulation and the torque from Reynolds stress, with the torque configured so as to maintain the roll. S3T theory explains this systematic correlation between the roll/streak structure and the perturbation torques maintaining it as a direct consequence of the straining of the perturbation field by the streak (Farrell & Ioannou 2012).

Having established that the streamwise vorticity in the outer layer is maintained *in situ* by systematic correlation of Reynolds stress torque with the roll circulation, we conclude that the SSP cycle in both NS and RNL operates in the outer layer in a manner essentially similar to that in the inner layer.

8. Discussion and conclusions

We have established that both NS and RNL produce a roll/streak structure in the outer layer and that an SSP is operating there despite the low shear in this region. It has been already shown that turbulence self-sustains in the log-layer in the absence of boundaries (Mizuno & Jiménez 2013) and that an SSP operates independently in the outer layer (Rawat *et al.* 2015). These results are consistent with our finding that an SSP cycle exists in both the inner layer and outer layer. RNL self-sustains turbulence at moderate Reynolds numbers in pressure-driven channel flow despite its greatly simplified dynamics when compared to NS. Remarkably, and consistent with the prediction of S3T that RNL turbulence is maintained by a small set of Lyapunov structures associated with the Lyapunov spectrum of the time-dependent streak, in the RNL system the turbulent state is maintained by a small set of structures with low streamwise wavenumber Fourier components (at $Re_\tau \approx 940$ with the chosen channel the SSP involves only the $k_x = 0$ streamwise mean and the next six streamwise Fourier components). In this way RNL produces a turbulent state of reduced complexity. RNL identifies an exquisitely contrived SSP cycle which has been previously identified to comprise the generation of the streak through lift-up by the rolls, the maintenance of the rolls by torques induced by the perturbations which themselves are maintained by an essentially time-dependent parametric non-normal interaction with the streak (rather than e.g. inflectional instability of the streak structure) (Farrell & Ioannou 2012). The vanishing of the Lyapunov exponent associated with the SSP is indicative of feedback regulation acting between the streaks and the perturbations by which the parametric instability that sustains the perturbations on the time-dependent streak is reduced to zero Lyapunov exponent, so that the turbulence neither diverges nor decays.

A remarkable feature of RNL turbulence is that it is supported by a streamwise constant SSP so that RNL turbulence does not imply a fundamental limitation to the streamwise extent of the streak. In a natural turbulent flow, fluctuations may be expected to produce deviations from this ideal streamwise constancy. Observations based on cross-spectral analysis determine the streamwise length of the VLSMs to be of the order of $30h$ in pipe flows and of the order of $10–15\delta$ in boundary layer flows (Jiménez & Hoyas 2008; Hellström *et al.* 2011; Lozano-Durán & Jiménez 2014*a*). However, Hutchins & Marusic (2007) argue that these are underestimates of their actual length, which can in fact be arbitrarily large. Moreover, when $k_x \neq 0$ perturbations are of large amplitude, observation may suggest that a $k_x = 0$ structure has non-zero wavenumber (cf. Hutchins & Marusic 2007). Consider for example the apparent lack of $k_x = 0$ structure in figure 8(*b*), despite the $k_x = 0$ structure of the underlying SSP.

The centrality of streamwise constant structure to the fundamental dynamics of wall turbulence is consistent with predictions of generalized stability theory (Farrell & Ioannou 1996*a*,*b*; Schmid & Henningson 2001) that both the optimal structure for growth of an initial perturbation (Butler & Farrell 1992; Farrell & Ioannou 1993; Reddy & Henningson 1993) as well as the optimal structure for producing a response by continuous forcing (Farrell & Ioannou 1996*a*; Bamieh & Dahleh 2001; Jovanović & Bamieh 2005; Cossu, Pujals & Depardon 2009; Sharma & McKeon 2013) are streamwise constant.

In this work, formation of roll/streak structures in the log-layer is attributed to the universal mechanism by which turbulence is modified by the presence of a streak in such way as to induce growth of a roll structure configured to lead to continued growth of the original streak. This growth process underlies the non-normal

parametric mechanism of the SSP that maintains turbulence (Farrell & Ioannou 2012). This universal mechanism neither predicts nor requires that the roll/streak structures be of finite streamwise extent, and in its simplest form it has been demonstrated that it supports roll/streak structures with zero streamwise wavenumber. From this point of view, the observed length of roll/streak structures is neither a primary nor necessary consequence of the SSP supporting them, but rather a secondary effect of disruption by the turbulence.

A distinction should be noted between mechanisms fundamentally related to streamwise constant processes and those which require that the streamwise constant structure also be time-independent. The mechanism we have advanced intrinsically requires that the streak be time-dependent for the parametric growth of perturbations to be supported. Because this fundamental mechanism of turbulence requires time dependence of the streamwise constant streak, it predicts that turbulence must be time-dependent and not exclusively spatially chaotic. It further implies that mechanisms based on critical layers and modal growth processes (Waleffe 1997; Hall & Sherwin 2010) cannot support turbulence by this mechanism because the temporal independence of the flow required for existence of critical layers and modal instability does not obtain in these turbulent flows.

Turbulence maintained in RNL exhibits a log-layer, although with different von Kármán constants depending on the truncation in streamwise wavenumber imposed on the RNL. However, it should be noted that judicious choice of the streamwise-varying components can produce von Kármán constants that are very close to those obtained in DNS (cf. Bretheim, Meneveau & Gayme 2015). Existence of a log-layer is a fundamental requirement of asymptotic matching between regions with different spatial scaling, as was noted by Millikan (1938). However, the exact value of the von Kármán constant does not have a similar fundamental basis in analysis. RNL turbulence, which is closely related to NS turbulence but more efficient in producing Reynolds stresses, maintains as a consequence a smaller shear, and therefore greater von Kármán constant.

In this work we have provided evidence that NS turbulence is closely related in its dynamics to RNL turbulence from the wall through the log-layer. Moreover, given that the dynamics of RNL turbulence can be understood fundamentally from its direct relation with S3T turbulence, we conclude that the mechanism of turbulence in wall-bounded shear flow can be insightfully related to the analytically tractable roll/streak/perturbation SSP that was previously identified to maintain S3T turbulence. We conclude that the severe restriction of the dynamics, coupled with the restricted support of the dynamics in streamwise wavenumber that are inherent in the RNL system, result in the establishment of a statistically steady turbulent state in which, while the maintained statistics differ in particulars from those of a DNS at the same *Re*, these systems share fundamental aspects of both structure and dynamics, and that this relation provides an attractive pathway to further understanding of wall turbulence.

Acknowledgements

REFERENCES

DEL ÁLAMO, J. C., JIMÉNEZ, J., ZANDONADE, P. & MOSER, R. D. 2004 Scaling of the energy spectra of turbulent channels. *J. Fluid Mech.* **500**, 135–144.

DEL ÁLAMO, J. C., JIMÉNEZ, J., ZANDONADE, P. & MOSER, R. D. 2006 Self-similar vortex clusters in the turbulent logarithmic region. *J. Fluid Mech.* **561**, 329–358.

BAKAS, N. A. & IOANNOU, P. J. 2013 Emergence of large scale structure in barotropic β-plane turbulence. *Phys. Rev. Lett.* **110**, 224501.

BAMIEH, B. & DAHLEH, M. 2001 Energy amplification in channel flows with stochastic excitation. *Phys. Fluids* **13**, 3258–3269.

BOUCHET, F., NARDINI, C. & TANGARIFE, T. 2013 Kinetic theory of jet dynamics in the stochastic barotropic and 2D Navier–Stokes equations. *J. Stat. Phys.* **153** (4), 572–625.

BRETHEIM, J. U., MENEVEAU, C. & GAYME, D. F. 2015 Standard logarithmic mean velocity distribution in a band-limited restricted nonlinear model of turbulent flow in a half-channel. *Phys. Fluids* **27**, 011702.

BULLOCK, K. J., COOPER, R. E. & ABERNATHY, F. H. 1978 Structural similarity in radial correlations and spectra of longitudinal velocity fluctuations in pipe flow. *J. Fluid Mech.* **88**, 585–608.

BUTLER, K. M. & FARRELL, B. F. 1992 Three-dimensional optimal perturbations in viscous shear flows. *Phys. Fluids* **4**, 1637–1650.

CONSTANTINOU, N. C., FARRELL, B. F. & IOANNOU, P. J. 2014a Emergence and equilibration of jets in beta-plane turbulence: applications of stochastic structural stability theory. *J. Atmos. Sci.* **71** (5), 1818–1842.

CONSTANTINOU, N. C., FARRELL, B. F. & IOANNOU, P. J. 2016 Statistical state dynamics of jet–wave coexistence in barotropic beta-plane turbulence. *J. Atmos. Sci.* **73** (5), 2229–2253.

CONSTANTINOU, N. C., LOZANO-DURÁN, A., NIKOLAIDIS, M.-A., FARRELL, B. F., IOANNOU, P. J. & JIMÉNEZ, J. 2014b Turbulence in the highly restricted dynamics of a closure at second order: comparison with DNS. *J. Phys.: Conf. Ser.* **506**, 012004.

COSSU, C., PUJALS, G. & DEPARDON, S. 2009 Optimal transient growth and very large-scale structures in turbulent boundary layers. *J. Fluid Mech.* **619**, 79–94.

DALLAS, V., VASSILICOS, J. C. & HEWITT, G. F. 2009 Stagnation point von Kármán coefficient. *Phys. Rev.* E **80**, 046306.

DRAZIN, P. G. & REID, W. H. 1981 *Hydrodynamic Stability*. Cambridge University Press.

FARRELL, B. F. & IOANNOU, P. J. 1993 Optimal excitation of three-dimensional perturbations in viscous constant shear flow. *Phys. Fluids* A **5**, 1390–1400.

FARRELL, B. F. & IOANNOU, P. J. 1996a Generalized stability. Part I. Autonomous operators. *J. Atmos. Sci.* **53**, 2025–2040.

FARRELL, B. F. & IOANNOU, P. J. 1996b Generalized stability. Part II. Non-autonomous operators. *J. Atmos. Sci.* **53**, 2041–2053.

FARRELL, B. F. & IOANNOU, P. J. 1999 Perturbation growth and structure in time dependent flows. *J. Atmos. Sci.* **56**, 3622–3639.

FARRELL, B. F. & IOANNOU, P. J. 2003 Structural stability of turbulent jets. *J. Atmos. Sci.* **60**, 2101–2118.

FARRELL, B. F. & IOANNOU, P. J. 2007 Structure and spacing of jets in barotropic turbulence. *J. Atmos. Sci.* **64**, 3652–3665.

FARRELL, B. F. & IOANNOU, P. J. 2008 Formation of jets by baroclinic turbulence. *J. Atmos. Sci.* **65**, 3353–3375.

FARRELL, B. F. & IOANNOU, P. J. 2009a Emergence of jets from turbulence in the shallow-water equations on an equatorial beta plane. *J. Atmos. Sci.* **66**, 3197–3207.

FARRELL, B. F. & IOANNOU, P. J. 2009b A stochastic structural stability theory model of the drift wave-zonal flow system. *Phys. Plasmas* **16**, 112903.

FARRELL, B. F. & IOANNOU, P. J. 2009c A theory of baroclinic turbulence. *J. Atmos. Sci.* **66**, 2444–2454.

FARRELL, B. F. & IOANNOU, P. J. 2012 Dynamics of streamwise rolls and streaks in turbulent wall-bounded shear flow. *J. Fluid Mech.* **708**, 149–196.

FARRELL, B. F. & IOANNOU, P. J. 2016 Structure and mechanism in a second-order statistical state dynamics model of self-sustaining turbulence in plane Couette flow. *Phys. Rev. Fluids*; (submitted, arXiv:1607.05020).

FARRELL, B. F., IOANNOU, P. J. & NIKOLAIDIS, M.-A. 2016 Instability of the roll/streak structure induced by free-stream turbulence in pre-transitional Couette flow. *Phys. Rev. Fluids*; (submitted, arXiv:1607.05018).

FLORES, O. & JIMÉNEZ, J. 2006 Effect of wall-boundary disturbances on turbulent channel flows. *J. Fluid Mech.* **566**, 357–376.

FLORES, O. & JIMÉNEZ, J. 2010 Hierarchy of minimal flow units in the logarithmic layer. *Phys. Fluids* **22**, 071704.

FOIAS, C., MANLEY, O., ROSA, R. & TEMAM, R. 2001 *Navier–Stokes Equations and Turbulence*. Cambridge University Press.

GAYME, D. F. 2010 A robust control approach to understanding nonlinear mechanisms in shear flow turbulence. PhD thesis, Caltech, Pasadena, CA, USA.

GAYME, D. F., McKEON, B. J., PAPACHRISTODOULOU, A., BAMIEH, B. & DOYLE, J. C. 2010 A streamwise constant model of turbulence in plane Couette flow. *J. Fluid Mech.* **665**, 99–119.

HALL, P. & SHERWIN, S. 2010 Streamwise vortices in shear flows: harbingers of transition and the skeleton of coherent structures. *J. Fluid Mech.* **661**, 178–205.

HAMA, F. R., LONG, J. D. & HEGARTY, J. C. 1957 On transition from laminar to turbulent flow. *J. Appl. Phys.* **28** (4), 388–394.

HAMILTON, K., KIM, J. & WALEFFE, F. 1995 Regeneration mechanisms of near-wall turbulence structures. *J. Fluid Mech.* **287**, 317–348.

HELLSTRÖM, L. H. O., MARUSIC, I. & SMITS, A. J. 2016 Self-similarity of the large-scale motions in turbulent pipe flow. *J. Fluid Mech.* **792**, R1.

HELLSTRÖM, L. H. O., SINHA, A. & SMITS, A. J. 2011 Visualizing the very-large-scale motions in turbulent pipe flow. *Phys. Fluids* **23**, 011703.

HUTCHINS, N. & MARUSIC, I. 2007 Evidence of very long meandering features in the logarithmic region of turbulent boundary layers. *J. Fluid Mech.* **579**, 1–28.

JIMÉNEZ, J. 1998 The largest scales of turbulent wall flows. In *CTR Annual Research Briefs*, pp. 137–154. Stanford University.

JIMÉNEZ, J. 2013 Near-wall turbulence. *Phys. Fluids* **25** (10), 101302.

JIMÉNEZ, J. & HOYAS, S. 2008 Turbulent fluctuations above the buffer layer of wall-bounded flows. *J. Fluid Mech.* **611**, 215–236.

JIMÉNEZ, J. & PINELLI, A. 1999 The autonomous cycle of near-wall turbulence. *J. Fluid Mech.* **389**, 335–359.

JOVANOVIĆ, M. R. & BAMIEH, B. 2005 Componentwise energy amplification in channel flows. *J. Fluid Mech.* **534**, 145–183.

KIM, J. & LIM, J. 2000 A linear process in wall bounded turbulent shear flows. *Phys. Fluids* **12**, 1885–1888.

KIM, J., MOIN, P. & MOSER, R. 1987 Turbulence statistics in fully developed channel flow at low Reynolds number. *J. Fluid Mech.* **177**, 133–166.

KIM, K. C. & ADRIAN, R. J. 1999 Very large-scale motion in the outer layer. *Phys. Fluids* **11**, 417–422.

KLINE, S. J., REYNOLDS, W. C., SCHRAUB, F. A. & RUNSTADLER, P. W. 1967 The structure of turbulent boundary layers. *J. Fluid Mech.* **30**, 741–773.

LOZANO-DURÁN, A., FLORES, O. & JIMÉNEZ, J. 2012 The three-dimensional structure of momentum transfer in turbulent channels. *J. Fluid Mech.* **694**, 100–130.

LOZANO-DURÁN, A. & JIMÉNEZ, J. 2014a Effect of the computational domain on direct simulations of turbulent channels up to $Re_\tau = 4200$. *Phys. Fluids* **26**, 011702.

LOZANO-DURÁN, A. & JIMÉNEZ, J. 2014b Time-resolved evolution of coherent structures in turbulent channels: characterization of eddies and cascades. *J. Fluid Mech.* **759**, 432–471.

MARSTON, J. B., CONOVER, E. & SCHNEIDER, T. 2008 Statistics of an unstable barotropic jet from a cumulant expansion. *J. Atmos. Sci.* **65** (6), 1955–1966.

MARUSIC, I., MCKEON, B. J., MONKEWITZ, P. A., NAGIB, H. M. & SREENIVASAN, K. R. 2010 Wall-bounded turbulent flows at high Reynolds numbers: recent advances and key issues. *Phys. Fluids* **22**, 065103.

MILLIKAN, C. B. 1938 A critical discussion of turbulent flows in channels and circular tubes. *Proceedings of the Fifth International Congress for Applied Mechanics*. Wiley.

MIZUNO, Y. & JIMÉNEZ, J. 2013 Wall turbulence without walls. *J. Fluid Mech.* **723**, 429–455.

NIKOLAIDIS, M.-A., FARRELL, B. F., IOANNOU, P. J., GAYME, D. F., LOZANO-DURÁN, A. & JIMÉNEZ, J. 2016 A POD-based analysis of turbulence in the reduced nonlinear dynamics system. *J. Phys.: Conf. Ser.* **708**, 012002.

PARKER, J. B. & KROMMES, J. A. 2013 Zonal flow as pattern formation. *Phys. Plasmas* **20**, 100703.

PARKER, J. B. & KROMMES, J. A. 2014 Generation of zonal flows through symmetry breaking of statistical homogeneity. *New J. Phys.* **16** (3), 035006.

RAWAT, S., COSSU, C., HWANG, Y. & RINCON, F. 2015 On the self-sustained nature of large-scale motions in turbulent Couette flow. *J. Fluid Mech.* **782**, 515–540.

REDDY, S. C. & HENNINGSON, D. S. 1993 Energy growth in viscous channel flows. *J. Fluid Mech.* **252**, 209–238.

SCHMID, P. J. & HENNINGSON, D. S. 2001 *Stability and Transition in Shear Flows*. Springer.

SHARMA, A. S. & MCKEON, B. J. 2013 On coherent structure in wall turbulence. *J. Fluid Mech.* **728**, 196–238.

SRINIVASAN, K. & YOUNG, W. R. 2012 Zonostrophic instability. *J. Atmos. Sci.* **69** (5), 1633–1656.

THOMAS, V., FARRELL, B. F., IOANNOU, P. J. & GAYME, D. F. 2015 A minimal model of self-sustaining turbulence. *Phys. Fluids* **27**, 105104.

THOMAS, V., LIEU, B. K., JOVANOVIĆ, M. R., FARRELL, B. F., IOANNOU, P. J. & GAYME, D. F. 2014 Self-sustaining turbulence in a restricted nonlinear model of plane Couette flow. *Phys. Fluids* **26**, 105112.

TOH, S. & ITANO, T. 2005 Interaction between a large-scale structure and near-wall structures in channel flow. *J. Fluid Mech.* **524**, 249–262.

TOWNSEND, A. A. 1976 *The Structure of Turbulent Shear Flow*, 2nd edn. Cambridge University Press.

WALEFFE, F. 1997 On a self-sustaining process in shear flows. *Phys. Fluids* **9**, 883–900.